Original Research Article

Assessing urban effects on the climate of metropolitan regions of Brazil - Preliminary results of the MCITY BRAZIL project

Amauri Pereira de Oliveira[1]*, Edson Pereira Marques Filho[2,3], Maurício Jonas Ferreira[1],
Georgia Codato[1], Flávia Noronha Dutra Ribeiro[1], Eduardo Landulfo[4], Gregori de Arruda Moreira[4,5],
Maxsuel Marcos Rocha Pereira[6], Primoz Mlakar[7], Marija Zlata Boznar[7], Eleonora Sad de Assis[8],
Daniele Gomes Ferreira[8], Mariana Cassol[2,3], João Francisco Escobedo[9], Alexandre Dal Pai[9],
José Ricardo de Almeida França[2], Demilson Assis Quintão[10], Flávia Dias Rabelo[1],
Luana Antunes Tolentino Souza[1], Wallace Pereira da Silva[2], Leonardo Moreno Domingues[1],
Maciel Piñero Sánchez[1], Lucas Cardoso da Silveira[1], Janet Valdes Vito[1]
[1]University of São Paulo (USP), São Paulo, SP, (BRAZIL)
[2]Federal University of Rio de Janeiro (UFRJ), Rio de Janeiro, RJ, (BRAZIL)
[3]Federal University of Bahia (UFBA), Salvador, BA, (BRAZIL)
[4]Institute of Nuclear Energy Research (IPEN), São Paulo, SP, (BRAZIL)
[5]Federal Institute of São Paulo (IFSP), Registro, SP, (BRAZIL)
[6]Federal University of Espírito Santo (UFES), Vitória, ES, (BRAZIL)
[7]MEIS d.o.o. (MEIS), Ljubljana, (SLOVENIA)
[8]Federal University of Minas Gerais (UFMG), Belo Horizonte, MG, (BRAZIL)
[9]State of São Paulo University (UNESP), Botucatu, SP, (BRAZIL)
[10]State of São Paulo University (UNESP), Bauru, SP, (BRAZIL)
E-mail: apdolive@usp.br
DOI : https://dx.doi.org/10.47204/EESR.1.1.2020.038-077

ABSTRACT

This work describes the MCITY BRAZIL Project. The project designed to assess urban effects on the climate of the major Brazilian cities and to systematize this procedure of investigation so it can be extended to other urban areas in Brazil. In this article, the implementations in the Metropolitan Regions of São Paulo and Rio de Janeiro are presented. A preliminary description of the surface radiation balance, surface energy balance, surface wind pattern, urban heat island and urban boundary layers are discussed by considering the surface observations carried out in the MCITY BRAZIL project from 2013 to 2014 in four micrometeorological towers in these two metropolitan regions. Despite nearly identical inputs of solar radiation at the top of the atmosphere, differences in the atmospheric attenuation and emissions, and in the surface albedo and emissions resulted in significant differences in surface radiation balance components between metropolitan regions and within each urban area. The diurnal evolution of the surface energy balance, friction velocity and carbon dioxide vertical fluxes observed during the field campaigns indicate important seasonal and spatial variations associated with the land use in both urban regions. Surface wind analyses for both metropolitan regions display similar seasonal and diurnal patterns as a result of the combination of large-scale systems and sea-breeze circulation present in both regions and modulated by topography. The urban heat island in São Paulo is greater than that in Rio de Janeiro as a result of different combinations of maritime and solar heating effects. The diurnal evolution of the urban boundary layer height and surface inversion layer top estimated simultaneously by rawinsonde and Lidar displays good agreement in both metropolitan regions. In São Paulo, daytime urban boundary layer height responds to the sensible heat flux at the surface. In Rio de Janeiro, despite of equivalent sensible heat flux, urban boundary layer is smaller due to the internal maritime boundary layer effects.   © 2020 Knowledge Empowerment Foundation

KEYWORDS

INTRODUCTION

The observational investigation of urban heat islands (UHI) and other urban effects on the climate of cities located in tropical and subtropical areas has received less attention than for cities located at higher latitudes; as a result, less is known about the urban climate in these regions[8,43,46,96,108-110]. This situation is particularly critical in the case of Brazil, where the urban fraction of the population grew from 36% in 1950 to 84% in 2010 (last demographic census), surpassing developed countries at the end of the 1980s and South American countries at the beginning of the 1990s. In addition, the urban population fraction of Brazil is expected to reach 91% in 2050, well above the expected fraction for the world (66%), developed countries (86%) and South American countries (89%)[123]. Therefore, the lack of scientific information about urban effects on the climate of tropical and subtropical cities has a very negative impact on policies to mitigate the adverse effects of urbanization.

It is important to emphasize that any actions taken to improve life quality in urban areas will have to be based on policies strongly supported by scientific knowledge about urban adverse effects on their climate. This knowledge will depend on observing and modeling a wide range of meteorological scales and on the effective integration of several interdisciplinary areas[15,59,82]. Moreover, if the IPCC scenarios are confirmed, a significant fraction of the population living in large conurbations of Brazil are likely to become more exposed to the adverse effects of climate change, further aggravating social and environmental problems and, the need for government financial resources to alleviate them[78]. There is observational evidence that the UHI of Brazilian cities has already increased the incidence of dengue, mortality, hospital admissions and suicide rate[7,12,116], contributed to the intensification of cloud convection, causing severe precipitation events that result in flooding, and a significant increase in the lightning activity[22,37,38,88,125]. The economic impacts of floods in the city of São Paulo are significant[54].

Following a worldwide trend reflecting the economic and social importance of the impact of urban population growth[8,16,64,107,109,117], the understanding based on observation of urban effects on the climate of Brazilian cities has improved. However, most of the observational work available in the literature is concentrated over a few urban areas located in the south and southeast states of Brazil[13,14,17,24,26,33,41,42,43,46,50,68,76, 81,85,93,94,99,121]. Even less observational work has been conducted in the northeastern[30] and northern[118] parts of the country. It should be emphasized that the above review about observational work on urban climate does not consider observational studies about air pollution in Brazilian cities. A review of this subject can be found in Andrade et al.[5].

Most of the observational works described above are limited to the analysis of conventional meteorological variables, mainly air and surface temperature, obtained by surface stations and satellite to monitor UHI of Brazilian cities[1,4,9,14,17,24,30,36,42,43,46,56,57,63,67,74,76,85,99, 121,122]. A much smaller number of works has characterized the behavior of the downward solar and atmospheric radiations at the surface[13,26,81,93] and surface wind circulation[94]. One study describes the vertical structure of the urban boundary layer, three studies focus on surface radiation, energy budget and anthropogenic heat[41-43]. None of them associates surface energy balance with boundary layer properties and vice versa.

It should be mentioned at this point that very few of these observational works have been used in the modeling of urban effects in Brazilian cities. This is a critical point because the assessment of urban effects on the climate of cities requires, besides observations, the use of numerical modelling[15,72,73,82,113,122]. Despite the efforts of the local research community, modelling studies from Brazil have not been strongly supported by observations, and in many cases, the numerical simulations of small-scale effects are either carried out using very simplified and coarse land use data or using numerical models that have not been fully evaluated for climate conditions representative of Brazilian cities and their biome[36,45,68,104].

The MCITY (Mega CITY) BRAZIL Project was designed to assess urban effects on the climate of the major Brazilian cities and to systematize this research so that it can be extended to other urban areas in Brazil. The focus of this project is to estimate observationally the major components of the surface energy budget (SEB) and associate them with the dynamic and

Original Research Article

thermodynamic properties of the planetary boundary layer (PBL) over urban areas of Brazil. This project is the first one in Brazil to address urban features in an integrated way and performing long-term measurements, and it is expected to provide relevant climate information about tropical and subtropical cities to local and international community by taking as reference other urban studies carried out in higher latitudes cities like METROMEX, BUBBLE and others[16,107,115,117]

The metropolitan regions of the cities of São Paulo (MRSP) and Rio de Janeiro (MRRJ) were chosen as the starting point in MCITY BRAZIL because they are the largest conurbations in Brazil. They are located at a similar subtropical zone (Figure 1), and together, they occupy approximately 13,733 km², with a population of 31.6 million inhabitants and a fleet of 10.6 million vehicles (TABLE 1). The city of São Paulo became a megacity in the early 90s. It reached 11.3 million inhabitants in 2010 and is expected to grow to 11.8 million inhabitants by 2020. The city of Rio de Janeiro reached 6.3 million inhabitants in 2010, and it is expected to grow to 6.7 million inhabitants by 2020[123]. In addition to social and economic importance, these two metropolitan regions are likely to contribute to climate change as significant sources of greenhouse gases (GHGs). According to Dodman[34], the emissions per capita of GHGs for the cities of São Paulo and Rio de Janeiro correspond respectively to 18.3% and 28.0% of the national emissions, which are estimated to be 8.2 tons of CO_2 equivalent. Most of the urban emissions in Brazil are due to transportation[29], although GHG emissions at the national level are basically due to rural activities (mainly deforestation and animal agriculture)[89].

TABLE 1 : Major social and economic features of the metropolitan regions of São Paulo (MRSP) and Rio de Janeiro (MRRJ)[59].

Features	MRSP	MRRJ
Number of cities	39	19
Area (km²)	8,051	5,682
Population	19,672.582	11,835,708
Number of vehicles	6,390,092	3,630,678

The main goal of this work is to describe the implementation of the MCITY BRAZIL Project in the MRSP and MRRJ. To complement this description, a preliminary characterization of the following is reported:

(a) surface radiation balance; (b) surface energy balance and turbulent fluxes; (c) surface wind pattern; (d) urban heat island; and (e) urban boundary layer. This characterization is based on observations from the surface stations in the two metropolitan regions from 2013 to 2014, and rawinsonde and Lidar measurements carried out during field campaigns in MRSP and MRRJ in 2013.

SITE, METHODS AND CLIMATE

The MCITY BRAZIL Project began in 2013 with the incorporation of a new turbulence measurement system into the previously existing micrometeorological platforms in the MRSP (PM IAG, "*Plataforma Micrometeorologica Instituto de Astronomia, Geofísica e Ciencias Atmosféricas*") and MRRJ (PM IGEO, "*Plataforma Micrometeorologica Instituto de GEOciências*"), along with the implementation of two new platforms in the MRSP (PM ITU,"*Plataforma Micrometeorologica ITUtinga*" and PM SFZ,"*Plataforma Micrometeorologica Secretaria da FaZenda*"). In the MRSP, all three platforms are placed at similar altitudes, varying from 741 m to 760 m above sea level (asl) (Figure 1a,c,e). In the MRRJ, the PM IGEO is located at sea level (Figure 1b,d,f). These platforms were set up to measure conventional meteorological variables, radiation components and turbulence to estimate the main components of the surface energy (SEB) and radiation (SRB) balance for five years. A complete description of the sensors implemented in the PM IAG, ITU, SFZ and IGEO is given in TABLE 2. In addition, four field campaigns (two in São Paulo and two in Rio de Janeiro) where rawinsondes were released every three hours over 10 consecutive days to characterize the urban boundary layer (UBL) during summer and winter were carried in 2013.

The topography of the MRSP (Figure 1e) is complex, which makes it very difficult to isolate the topographic effects on the surface wind pattern from the one induced by the land use[94]. The entire urban portion of the MRSP is in a plateau approximately 700 m asl ("*Paulista* Plateau"), limited at the north and northwest by a chain of ridges approximately 1400 m asl. The MRSP is characterized by three major valleys:
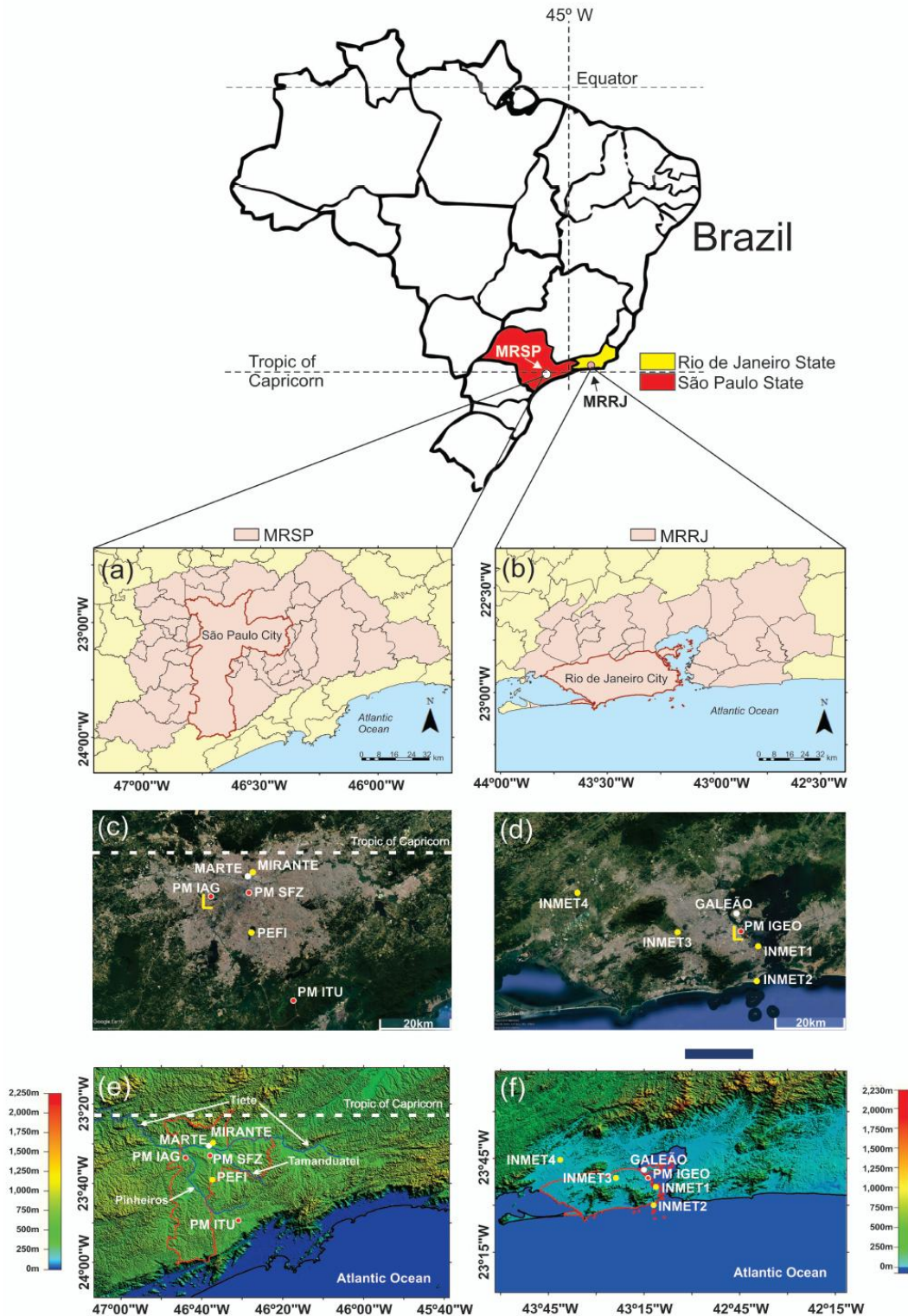
Original Research Article

Figure 1 : Locations of municipalities in the Metropolitan Regions of (a) São Paulo (MRSP) and (b) Rio de Janeiro (MRRJ) with the cities themselves indicated with red contours. Positions of (c) PM IAG, PM SFZ, PM ITU (red dots), "*Campo de Marte*" airport (MARTE, white dot) and climatological stations MIRANTE and PEFI (yellow dot) in the MRSP and (d) PM IGEO, "*Galeão*" airport (GALEÃO, red dot) and climatological stations INMET1-4 (yellow dot) in the MRRJ. Topography indicated in (e) MRSP and (f) MRRJ is based on the highest-resolution topographic data (3-arc-second Resolution -90 m) generated from NASA's Shuttle Radar Topography Mission (SRTM), available at https://www2.jpl.nasa.gov/srtm/. Lidar position are indicated by L in (c) and (d).

Original Research Article

the *Tiete* River valley, oriented in the east-west direction; the *Tamanduatei* River valley, oriented in the northwest-southeast direction, and the *Pinheiros* River valley, oriented in the northeast-southwest direction. In the south, there are large water bodies composing the *Billings* Dam system, which occupies 582.8 km^2[95]. Similarly, the topography of the MRRJ is rather complex (Figure 1f). It is characterized by chain of mountains oriented in the east-west direction. The urban areas are surrounded by mountains, with high cliffs concentrated at the north[39]. There are high-elevation mountains at the north and south and along the shoreline. The Guanabara Bay region is sheltered by the mountains at the north and isolated cliffs at the south. Land use of both metropolitan regions are very complex and describing them is rather cumbersome task due to the lack of data. In the case of the MRSP the location of the platforms was chosen to represent three classes of land use: suburban (PM IAG), urban (PM SFZ) and rural (PM ITU). In the case of the MRRJ the location of platform represents the suburban class (PM IGEO).

Site description

Suburban site PM IAG

The PM IAG (23°33'34"S; 46°44'01"W; 744 m asl) is composed of a 10-m tower located in the center of a concrete platform on the top of a 4-story building (Figure 2a), 17 m above ground level (agl) in the University of São Paulo campus, located in the western part of São Paulo City. Within a 1 km-radius the PM IAG area (Figure 3a outer circle) is occupied by 25.4 % of trees, 64.1 % of impervious building and streets, 7.3 % by grass, shrub and scrub, 2.3 % of water from the university rowing track (Figure C1a inner white circle, TABLE C1, Appendix C). Increasing to 3 km-radius, the amount of land covered by trees drops to 5.5 %, grass, shrub and scrub to 2.1 %, impervious building and streets rises to 89.1%, and water to 2.3 % due to the incorporation of the *Pinheiros* river (Figure C1a outer black circle, TABLE C1, Appendix C). The Local Climate Zone classification (Figure 3b inner circle) indicates that PM IAG is LCZ 6 which indicates

TABLE 2 : Sensors set up on the micrometeorological platforms of the MCITY BRAZIL Project implemented in 2013.

Description, model, manufacturer	Accuracy or precision	Variable	Height* (m)				Sample Freq. rate (Hz)
			IAG	ITU	SFZ	IGEO	
3D sonic anemometer and gas analyzer, IRGASON, CSI.	1 mm s^{-1} 1 mm s^{-1} 0.5 mm s^{-1} 0.025°C 0.2 mg m s^{-3} 3.50 mg m^{-3} 0.15°C 1.5 KPa	$u, v, w, Ts,$ ρ_{H2O}, ρ_{CO2}	8.40 (135°)^A	9.55 (270°)^A	8.00 (270°)^A	8.50 (0°)^A	10
Temperature sensor, Vaisala		T	7.50	7.50	8.20	8.00	
Pressure sensor Vaisala		p	7.00	7.00	5.85	8.00	
Net radiometer, CNR4, Kipp-Zonen Inc.	5%	$R_N, SW_{DW}, SW_{UP},$ LW_{DW}, LW_{UP}	7.00	9.35	5.80	1.20	
Temperature and relative humidity sensor, CS215, CSI	0.4 °C, 0.4%	T, RH	9.60			8.0	
			8.45	1.60	1.55	6.0	
			1.70			3.0	
Infrared surface temperature, SI111, CSI.	0.2 °C	T_{SRF}	5.00	-	3.85	5.0	
3-cup anemometer and vane, 034B, MetOne Instruments Inc	±0.11 ms^{-1}, 0.7998 ms^{-1} ±4°, 0.5°	Vel, Dir	9.50	9.70	8.00	6.0	0.5
3-cup anemometer, 014A, MetOne Instruments Inc	1.5%	Vel	5.30	-	-	3.0	
			2.80	-	-		
Tipping bucket rain gauge, TB4 385, CSI	2-3% (1 inch)	$prec$	1.50	1.50	1.48	1.2	
Barometric pressure sensor, CS106, CSI	±0.3 mb	p	1.50	1.50	-	-	
PAR Sensor, Lite, Kipp-Zonen	5%	SW_{PAR}	1.50	9.70	-	1.2	
UV Sensor, CUV5, Kipp-Zonen	1%	SW_{UV}	1.50	-	-	1.2	
Soil Heat Flux meter, HFP01, CSI	-15% to 5%	G	-0.05	-0.05	-	-0.05	
Soil Temperature, 107, CSI	-0.4%	T_G	-0.05	-0.05	-	-	
Datalogger, CSI	-	-	CR5000	CR3000	CR3000	CR5000	-

(*) **Above the platform surface.** (^{A}) **Orientation (Geographic direction) of the 3D Sonic Anemometer. CSI, Campbell Scientific Inc.**
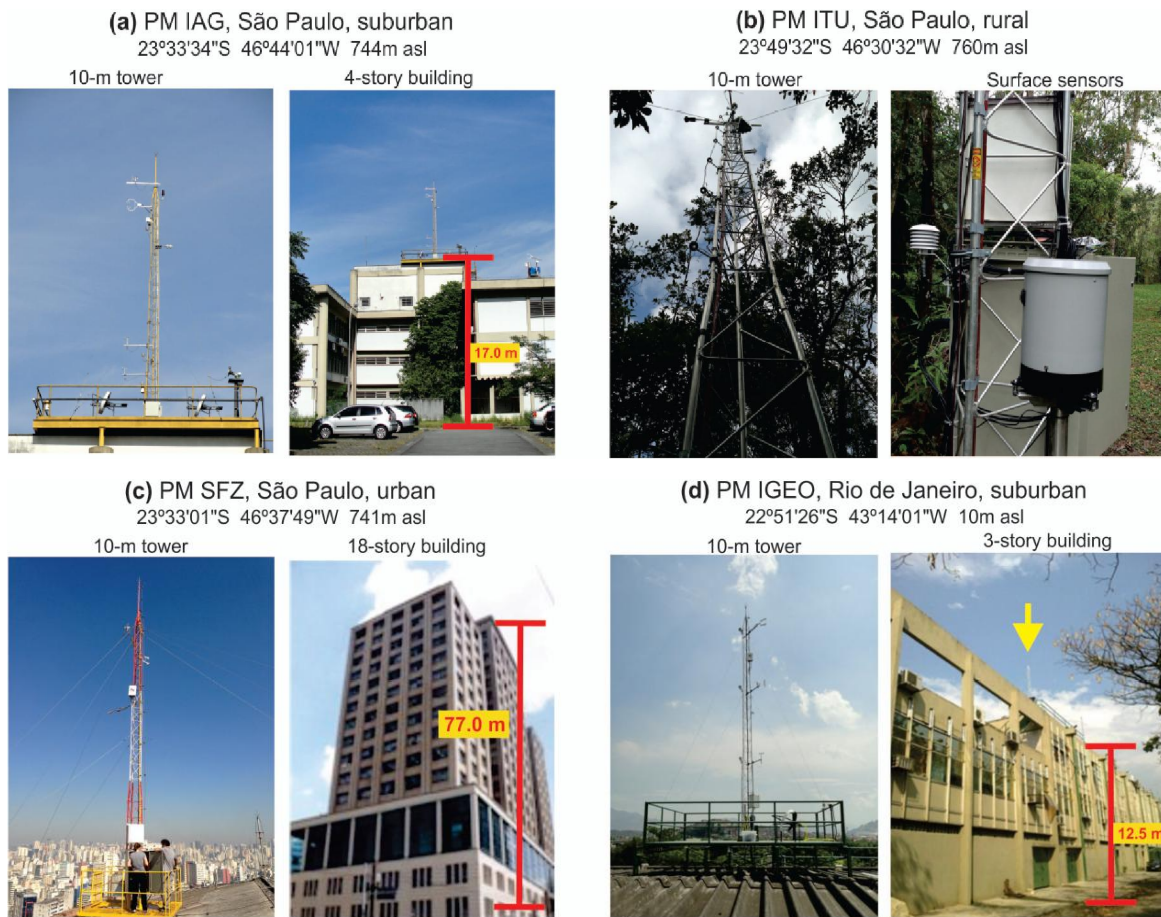
Original Research Article

(a) PM IAG, São Paulo, suburban
23°33'34"S 46°44'01"W 744m asl
10-m tower   4-story building

(b) PM ITU, São Paulo, rural
23°49'32"S 46°30'32"W 760m asl
10-m tower   Surface sensors

(c) PM SFZ, São Paulo, urban
23°33'01"S 46°37'49"W 741m asl
10-m tower   18-story building

(d) PM IGEO, Rio de Janeiro, suburban
22°51'26"S 43°14'01"W 10m asl
10-m tower   3-story building

Figure 2 : Main features of the (a) PM IAG, (c) PM ITU, (c) PM SFZ and (d) PM IGEO.

suburban land use (TABLE B1, Appendix B). Topography is slightly sloping to the *Pinheiros* river valley, with elevation varying 718 m asl in the north to 782 m asl in south of the 500 m-radius circle centered in PM IAG (Figure 3c). The spatial distribution of the buildings, indicated by the green areas in Figure 3d, was estimated from digital maps and using a QGIS algorithm developed by Ferreira et al.[40]. It indicates that most buildings, within a 500 m-radius, have 3-4 stories and are sparsely distributed, with mean building height of 6.6 m (TABLE B1, Appendix B).

Rural site PM ITU

The PM ITU (23°49'32"S; 46°30'32"W; 760 m asl) consists of a 10-m tower set up at the surface level in a vegetated area (Figure 2b) located south of the MRSP on the border between the cities of *São Bernardo do Campo* and *Cubatão*. It is situated in *Itutinga Pilões* State Park and in an area of reforestation of the Brazilian Atlantic Forest[105]. Within a 1-km radius the PM ITU area (Figure 4a,b outer

circles) is occupied by 87.6 % of trees, 4.9 % of grass, shrub and scrub, 4.5 % of water from the Billings Dam, and 2 % of impervious roads (Figure C1b inner white circle, TABLE C1, Appendix C). Increasing to 3-km radius, the amount of land covered by trees drops to 69.9 %, water rises to 21.2 %, grass and shrub to 6 %, and impervious surface to 2.5 % (Figure C1b outer black circle, TABLE C1, Appendix C). The Local Climate Zone classification (Figure 4b) indicates that PM ITU belongs to LCZ A which indicates rural land use (Figure 4b inner circle, TABLE B1, Appendix B). Within 1-km radius circle, the topography is characterized by gentle hills (mean height 50 m) (Figure 4c).

Urban site PM SFZ

The PM SFZ (23 33'01"S; 46 37'49"W;741 m asl) comprises a 10-m tower set up in the center of a metallic platform on the top of a 18-story building (Figure 2c), 77 m agl in downtown São Paulo City. Within 1-km radius the PM SFZ area (Figure 5a outer circle) is occupied by 5.6 % of trees, 88.6 % of impervious
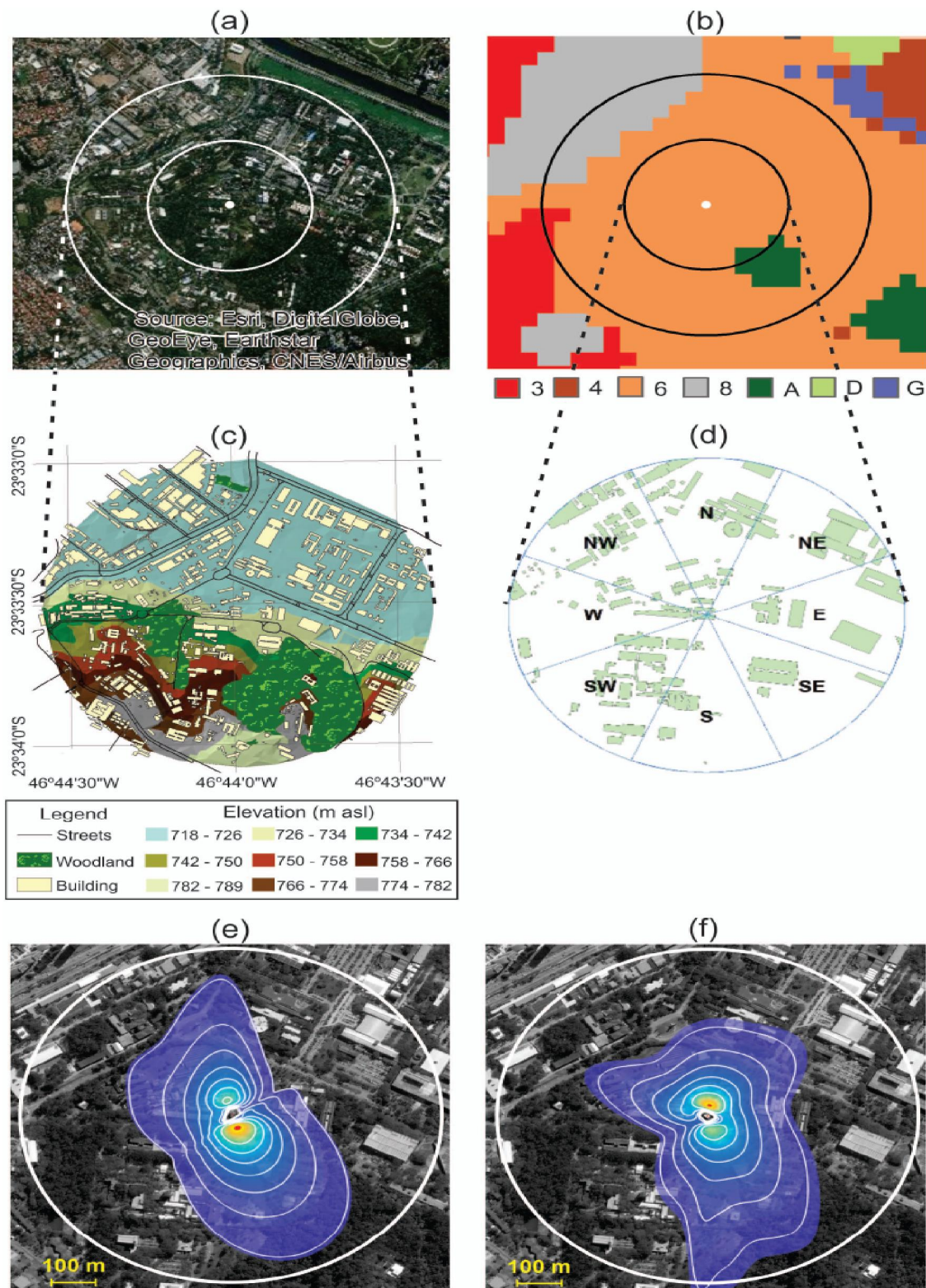
Original Research Article

Figure 3 : PM IAG (a) land use, (b) LCZ, (c) land use and topography, (d) building distribution, and footprint during (e) 1ˢᵗ and (f) 4ᵗʰ campaigns of 2013. Building distribution area within a 500 m radius in (d) corresponds to inner circle areas in (a) and (b) and footprint areas within the white circles in (e) and (f). Land use and topography within a 1-km radius in (c) correspond to outer circles in (a) and (b). Footprints in (e) and (f) obtained from Flux Footprint Prediction model developed by Kljun et al.[65], correspond to areas delimited by white lines ranging from (e) 10 to 70 % and (f) 10 to 60% (© CNES (2018) Distribution Airbus DS). White circles in (e) and (f) have radius equal to 500 m.
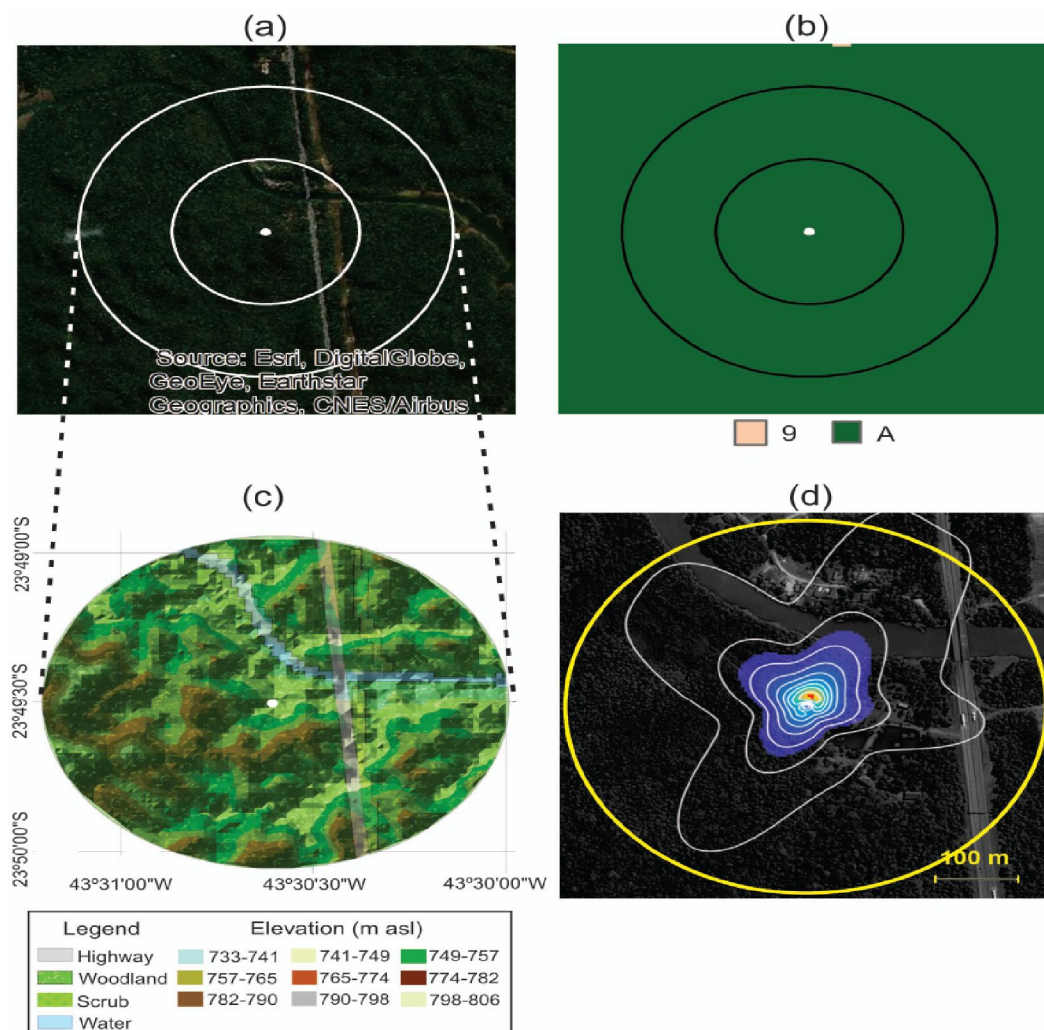
Figure 4 : PM ITU (a) land use, (b) LCZ, (c) land use and topography and (d) footprint during 4th campaign of 2013. Legend and elevation at right in the bottom correspond to land use and topography in (c). In (d) footprint, using Flux Footprint Prediction model developed by Kljun et al.[65], correspond to areas delimited by white lines indicating increase of 10 % up to 90 % (© CNES (2018) Distribution Airbus DS). The yellow circle in (d) has radius equal to 300 m.

building and streets, 3.6 % of grass, shrub and scrub, and 0.9 % of water (Figure C1c inner white circle, TABLE C1, Appendix C). Increasing to 3 km-radius area, the land covered by trees drops to 2.8 %, and grass, shrub and scrub to 2.1 %, impervious building and streets rises to 96.1%, and no significant water is found (Figure C1c outer black circle, TABLE C1, Appendix C). The Local Climate Zone classification (Figure 5b inner circle) indicate PM SFZ is LCZ 8 which indicates urban land use (TABLE B1, Appendix B). Topography is slightly sloping to the *Tamanduateí* river valley, oriented in the N-S direction at east of the PM SFZ, with 718 m asl in the valley center the surface elevation increases to 782 m asl in the west and to 762 m asl in the east (Figure 5c). The spatial distributions of

buildings in the 500-m radius circle area centered in PM SFZ, indicated by the gray areas in Figure 5d, was estimated from digital maps using a QGIS algorithm developed by Ferreira et al.[40]. It indicates that the building-size distribution around PM SFZ is more heterogeneous and concentrated, with mean building heights of 16.4 m, well below the height of PM SFZ (TABLE B1, Appendix B).

Suburban site PM IGEO

The PM IGEO (22°51'26"S; 43°14'01"W; 10 m asl) consists of a 10-m tower set up in the center of a metallic platform located on the top of a 3-story building (Figure 2d), at 12.5 m agl in the Federal University of Rio de Janeiro campus in the *Fundão* Island (Figure 1d,f). Within 1-km radius the PM IGEO area (Figure
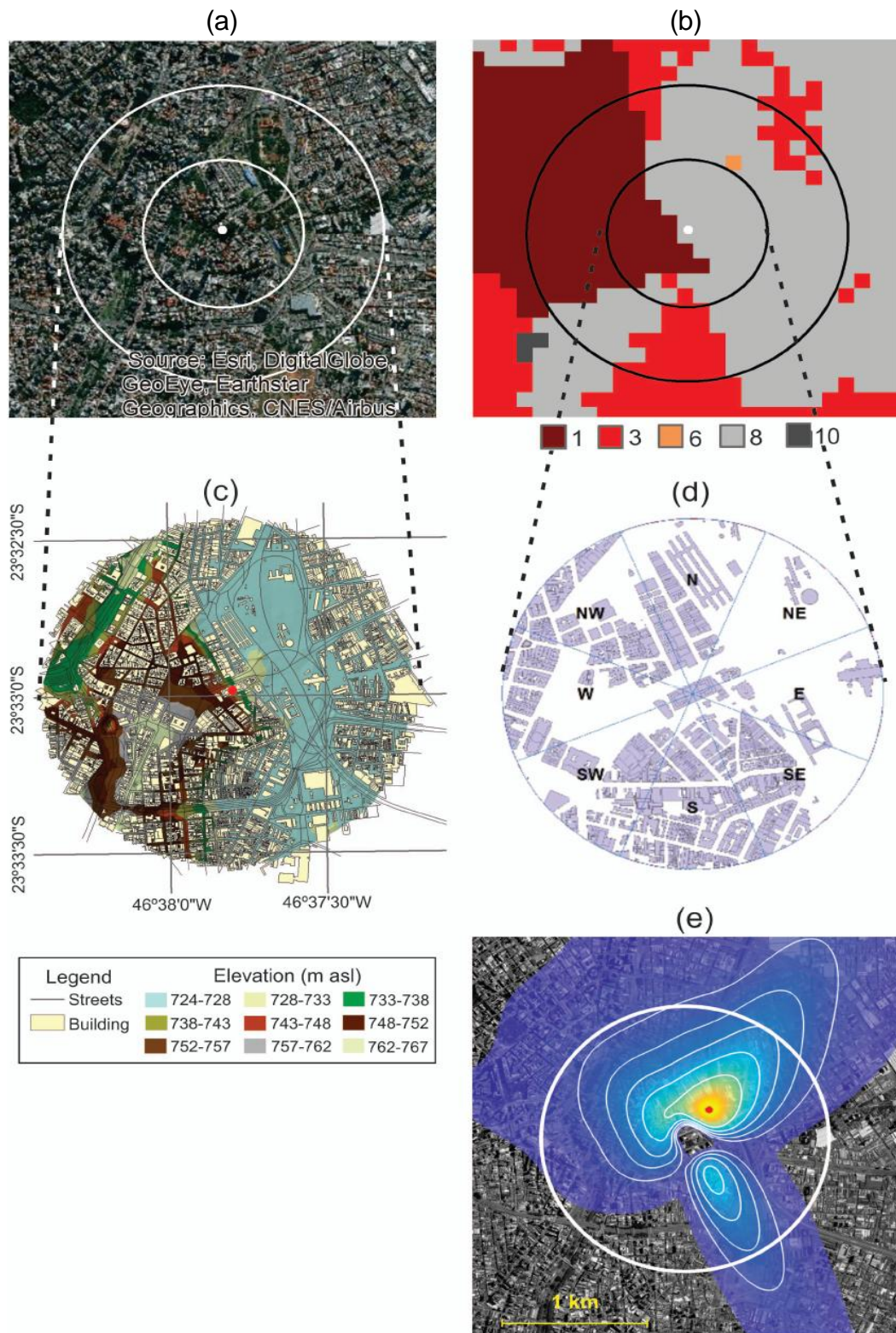
Original Research Article

Figure 5 : PM SFZ (a) land use, (b) LCZ, (c) land use and topography, (d) building distribution, and (e) footprint during 4ᵗʰ campaign of 2013. Building distribution within a 500 m radius in (d) correspond to inner circle areas in (a) and (b). Land use and topography within a 1000 m radius in (c) correspond to outer circles in (a) and (b) and white circle area in (e). In (e) footprint, using Flux Footprint Prediction model developed by Kljun et al.[65], correspond to areas delimited by white lines indicating increase of 10 % up to 50 % (© CNES (2018) Distribution Airbus DS). White circle in (d) has radius equal to 1 km.

6a outer circle) is occupied by 14.9 % of trees, 47.0 % of impervious building and streets, 10.4 % of grass, shrub and scrub, and 21.2 % of water (Figure C2a inner white circle, TABLE C1, Appendix C). Increasing to 3 km-radius area, the land covered by trees drops to 7.5 %, and grass, shrub and scrub to 2.8 %, impervious building and streets rises to 51.1%, and water to 33.2 % of (Figure C2a outer black circle, TABLE C1, Appendix C). The Local Climate Zone classification (Figure 6b inner circle) indicate PM IGEO is LCZ 6 which indicates suburban land use (TABLE B1, Appendix B). Topography of the area around PM IGEO is relatively flat with very gentle hills (Figure 6c). Unfortunately, digital maps are not available, and it is not possible to get a more precise information about the spatial distribution of buildings as in the other sites. However, LCZ classification indicated that within a 300-m radius circle area around the PM IGEO the building heights vary from 2.4 m to 16.7 m, with a mean value equal to 6.1 m (TABLE B1, Appendix B). Therefore, there is not significant obstacle affecting the flow around this site.

Supporting sites

Meteorological sites

In the case of the MRSP, the climate is characterized by 30-years normal based on observations carried out from 1961 to 1990 (TABLE A2, Appendix A) at the PEFI (23°39'04"S; 46°37'20"W; 799 m asl) and MIRANTE (23°29'47"S; 46°37'11"W; 792 m asl) climatological stations located in southern and northern São Paulo. The PEFI (*Parque Estadual das Fontes do Ipiranga*) belongs to the University of São Paulo, and it is the oldest climate station in São Paulo City (observations began in 1933). The MIRANTE (*Mirante de Santana*) belongs to the Brazilian Institute of Meteorology network ("*Instituto Nacional de Meteorologia do Brasil*", INMET, observations began in 1945. The Local Climate Zone classification indicates PEFI as LCZ A and MIRANTE as LCZ 3 (Figure B1a,b right panel, TABLE B1, Appendix B). PEFI can be classified as suburban and MIRANTE as urban (Figure C1d-e, TABLE C1, Appendix C).

Similarly, the climate of the MRRJ is characterized by 30 years normal based on carried out from 1961 to 1990 at the INMET1 (22°53'43"S; 43°11'11"W; 11 m) climatological station (TABLE A2, Appendix A). The INMET1 is in the urban area of Rio de Janeiro City near to the shoreline and also belongs to the Brazilian Institute of Meteorology network. The Local Climate Zone classification indicates INMET1 is LCZ 3 (Figure B1c inner circle in the right panel, TABLE B1, Appendix B). INMET1 can be classified as suburban (Figure C2b, TABLE C1, Appendix C).

Three more climatological stations from the Brazilian Institute of Meteorology network were used in this work to estimate the UHI: INMET2, INMET3 and INMET4. Meteorological data used here correspond to observations carried from July 1st, 2013 to December 31st, 2014 (TABLE A2). Details about these measurements can be found in TABLE A1 in the Appendix A. Station INMET2 (22°59'18"S; 43°11'26"W, 26 m asl) is in *Copacabana* neighborhood, located 200 m from the shoreline (Figure B1d left panel, Appendix B). Station INMET3 (22°51'41"S; 43°24'41"W; 30 m asl) is in *Deodoro* neighborhood, 17 km far from the shoreline (Figure B1e left panel, Appendix B). Station INMET4 (22°45'28"S; 43°41'05"W; 35 m asl) is in *Seropédica Agrícola* neighborhood, located 21 km from the shoreline (Figure B1f left panel, Appendix B). The Local Climate Zone classification indicates INMET2 is LCZ G, INMET3 LCZ 6 and INMET4 LCZ D (Figure B1d-f inner circle in the right panel, TABLE B1, Appendix B). INMET2 can be classified as urban, INMET3 as suburban and INMET4 as rural (Figure C2c-e, TABLE C1, Appendix C).

Sounding and lidar sites

Four field campaigns carried out in 2013 provided vertical profiles of temperature, relative humidity, wind velocity and wind direction, from rawinsondes released every three hours over 10 consecutive days in São Paulo (February 19-28 and August 6-15) and Rio de Janeiro (March 12-21 and July 9-19). These campaigns were designed to sample the atmospheric conditions during summer (February, March) and winter (July, August) in both metropolitan regions. In São Paulo, all rawinsondes were released at the "*Campo de Marte*" Airport (Figure 1c). In Rio de Janeiro, they were released at the "*Galeão*" Airport (Figure 1d). The
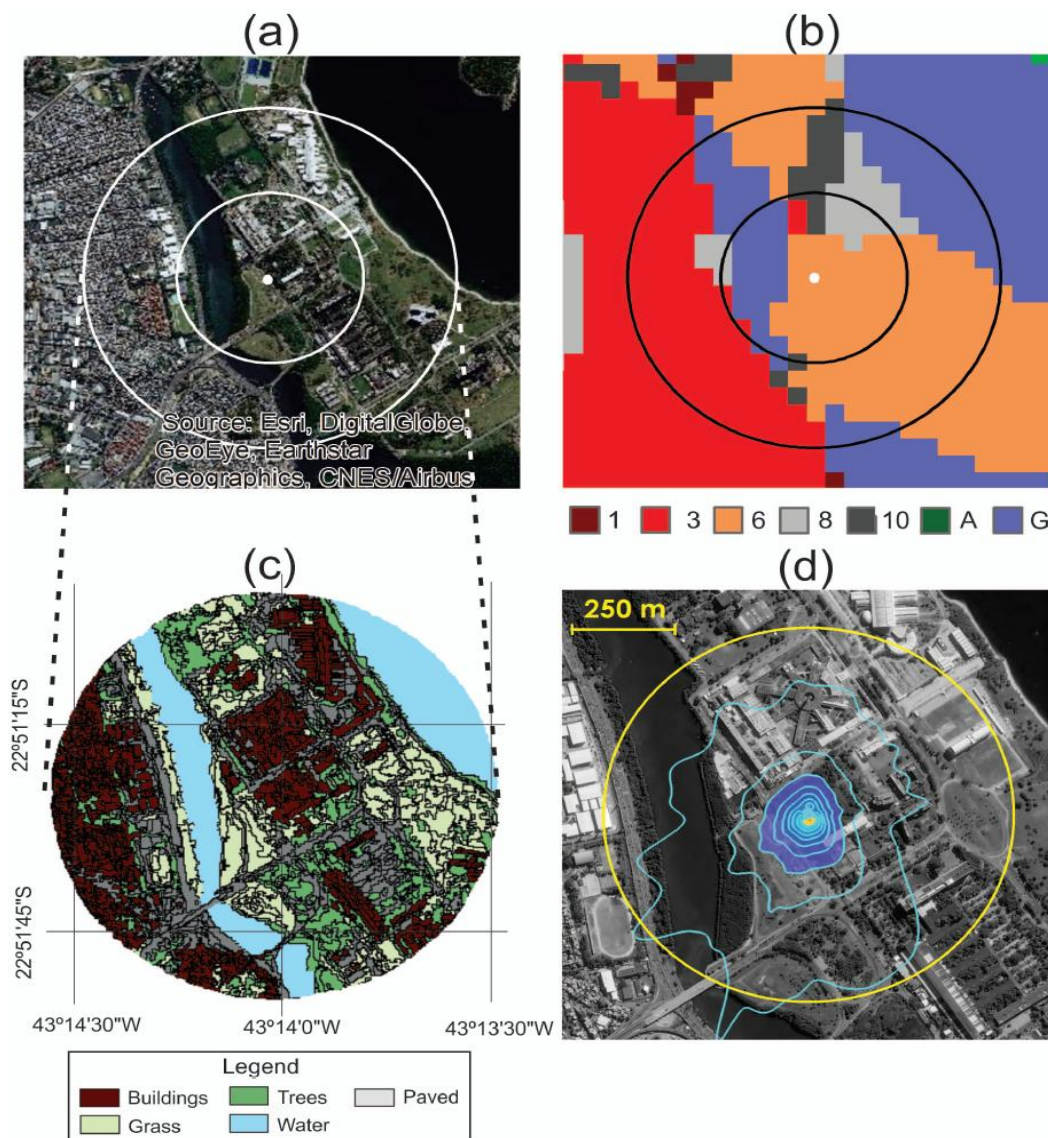
Original Research Article

Figure 6 : PM IGEO (a) land use, (b) LCZ, (c) land use and topography, and (d) footprint during the 4th campaign of 2013. Land use within a 1000 m radius in (c) corresponds to outer circles in (a) and (b). In (d) footprint, using Flux Footprint Prediction model developed by Kljun et al.[65], corresponds to areas delimited by blue lines indicating increase of 10 % up to 90 % (© CNES (2018) Distribution Airbus DS). Yellow circle in (d) has radius equal to 1 km.

"*Campo de Marte*" Airport is located 11.6 km far from PM IAG, 4.6 km from PM SFZ and 37.4 km from PM ITU. The "*Galeão*" Airport is located 5.3 km from PM IGEO. In both airports, the sounding system consisted of radiosonde model RS92-GSP and a DIGICORA III, manufactured by Vaisala Inc. During these campaigns, a Raman Lidar System MSP-lidar 2 monitored the PBL height at the University of São Paulo campus approximately 1 km from PM IAG, (Figure 1c) in São Paulo City and at the Federal University of Rio de Janeiro campus (in the PM IGEO) in Rio de Janeiro City (Figure 1d). Land use and topography of these sites are described in the next sections.

Methods

Surface radiation balance

The SRB components are estimated here considering a control volume involving the urban canopy. In this case, all energy fluxes across the horizontal faces of this volume are assumed constant so that the energy conservation can be expressed as:

$$R_N = SW_{DW} + SW_{UP} + LW_{DW} + LW_{UP} \tag{1}$$

where R_N is the net radiation at the surface, SW_{DW} and SW_{UP} are shortwave downward and upward radiation,

and LW_{DW} and LW_{UP} are longwave downward and upward radiation. The sign convection adopted here is positive (negative) whenever the energy flux is upward (downward) with respect to the surface. All four SRB components and net radiation are measured simultaneously with a sampling frequency of 0.5 Hz and store as 5-minutes average in all platforms using net radiometer model CNR4 at the four eddy covariance sites (TABLE 2). These 5-minutes values are checked, and spurious values caused by malfunctioning, shadows and reflection effects from nearby obstacles and rainy days are removed. Details about radiation sensors set up can be found in the TABLE A1 in Appendix A. The extraterrestrial solar radiation (*SWTOP*) was estimated accordingly to Iqbal[62] and considering the solar constant as equal to 1366 W m⁻². The resulting six series (SW_{DW}, SW_{UP}, LW_{DW}, LW_{UP}, R_N, SW_{TOP}) are used to estimate monthly average hourly values considering the observation carried out from July 1st, 2013 to December 31st, 2014.

Surface energy budget and turbulent fluxes

The SEB in an urban area can be estimated by considering a control volume involving the urban canopy. In this case, all energy fluxes across the horizontal faces of this volume are assumed constant so that the energy conservation can be expressed as:

$$R_N + Q_F = H + LE + \Delta QS + A \tag{2}$$

where Q_F is the anthropogenic heat, H and LE are the vertical turbulent energy fluxes of sensible and latent heat, ΔQS is the energy flux store in the canopy (including soil heat flux G) and A is the energy flux advection[90].

Vertical turbulent fluxes of sensible and latent heat and carbon dioxide are estimated according to the eddy-covariance method. A sonic anemometer coupled to a gas analyzer provides times series of sonic air temperature (T_S), water vapor density (ρ_{H2O}), carbon dioxide concentration (ρ_{CO2}) and the three components of wind speed (u, v, w) measured simultaneously with a sampling frequency of 10 Hz (TABLE 2). According to the eddy-covariance (EC) method, the turbulent vertical fluxes of sensible and latent heat and carbon dioxide are estimated according to the following:

$$H = \rho\, c_P \overline{(T'w')} \tag{3}$$

$$LE = L_V \overline{(\rho'_{H20} w')} \tag{4}$$

$$F_{CO2} = \overline{(\rho'_{co2} w')} \tag{5}$$

where ρ is air density, c_p is the specific heat at constant air pressure, and L_V is the water vapor latent heat. In expression (3), the air temperature (T) is estimated from the sonic temperature (Ts), water vapor density and atmospheric pressure[10].

The friction velocity is evaluated by applying EC method to estimate vertical turbulent fluxes of horizontal components of wind speed as follows:

$$u_* = \left[\overline{(u'w')}^2 + \overline{(v'w')}^2 \right]^{0.25} \tag{6}$$

The turbulence measurements at the PM IAG, PM SFZ, PM ITU and PM IGEO are performed using sonic anemometer model IRGASON, manufactured by Campbell Scientific Inc (TABLE 2) set up on 10-m micrometeorological towers. In the PM IAG turbulence measurements are carried out at 25.4 m agl, in the PM ITU at 9.6 m agl, in the PM SFZ at 85.0 m agl and in the PM IGEO at 22.7 m agl (TABLE A1 in the Appendix A). In the case of PM ITU turbulence sensors are located 2.5 m above the canopy top (7.1 m agl). Soil heat fluxes are measured in PM IAG and PM ITU using soil fluxmeter, model HFP01, CSI, set up at 5 cm below the surface (TABLE A1 in the Appendix A). The soil heat measurements are performed with a sample frequency of 0.5 Hz and stored as 5-minutes mean.

All turbulent fluxes and other statistics in this work are estimated considering the algorithm developed by the Laboratory of Micrometeorology of IAG (USP) and named MBFlux (MCITY Brazil Flux)[80,86,92,120]. Analysis of the turbulent fluxes include: (i) Webb correction, (ii) a procedure to remove spikes, (iii) linear detrending, (iv) skewness and kurtosis thresholds, (v) a procedure to classify and remove non-stationary turbulent data, and (vi) a procedure to remove tower blocking effects and (vii) rain effects[10,80,126]. In addition, the performance of the turbulence sensors was verified using (viii) the flags provided by the manufacturer[23], and by taking into consideration (ix) tilting effects caused by topography using a planar fit[44] or double rotation[127] procedures. The time interval used to calculate fluxes was 30 minutes. Each campaign thus corresponds to 480 data points. For the observations carried out at the PM IAG during the 1st and 4th campaigns, only 59.5% of the 962 blocks are considered valid after

Original Research Article

enforcing (i)-(ix). During the 4th campaign, only 39% of the 481 blocks of data measured at the PM ITU are considered valid. Observations gathered at the PM SFZ show the largest fraction of valid data (66.5%) for all the criteria used here. More details about MBFlux performance can be found in the Appendix D.

To avoid individual building effects presents in the roughness sublayer, turbulence measurements must be carried out in the inertial layer above the blending height. In practical terms blending heights correspond to 2-4 times mean building heights[124]. Therefore, it is important to estimate the geometric properties of buildings and other obstacles in the vicinity of sites. Since the spatial distributions of the buildings are highly heterogeneous in PM IAG and PM SFZ, they were organized into 8 consecutive sectors of 45° centered on and identified by the corresponding geographic direction. The radial distribution of the 45° sector average for the building geometric properties -building height (z_H) and horizontal fraction of built area to the total area (λ_P) -were estimated by considering the 500 m radius circles centered on the PM IAG and PM SFZ (Figures 3d and 5d) using digital maps and a QGIS algorithm developed by Ferreira et al.[40].

The distribution of building heights as a function of the 45°-sector indicate a mean building height of 8.36 m in the case of the PM IAG and a mean building height of 19.75 m for the PM SFZ (Figure 7a). In the case of the PM IAG, the building heights are more homogeneous than those of the PM SFZ, but both regions' building heights vary with the sector direction. The radial distribution of the horizontal fraction of the built area to the total area (Figure 7b) in the vicinity of the PM IAG is different from that in the PM SFZ (Figure 7b). With mean values equal to 0.18 (PM IAG) and 0.33 (PM SFZ) the horizontal fraction of built area corroborated with the land use inventory analyses, which yield an urban character for the PM SFZ and a suburban character for the PM IAG (TABLE C1, Figure C1a-b, Appendix C).

The zero-plane displacement height (z_D) and aerodynamic roughness length (z_0) were estimated based on morphometric proprieties of platforms in the MRSP[53] and aerodynamic methods[32,52] for the platform in the MRRJ. In the case of the MRSP, the average z_D (Figure 7c) and z_0 (Figure 7d) are,

respectively 4.2 m and 1.2 m for the PM IAG, and 9.9 m and 2.0 m for the PM SFZ. These estimates are based on Kutzbach[69] expression for PM IAG, Macdonald et al.[77] and Hanna and Chang[55] expressions for PM SFZ. In the case of the PM ITU z_D and z_0 equal to 0.8 m and 11.9 m respectively were estimated in terms of tree canopy mean height and the expression proposed by Hanna and Chang[53] and Raupach et al.[102]. In the case of PM IGEO z_D was estimated considering the free convection similarity relation between the standard deviation of vertical wind velocity and the kinematic sensible heat flux, when H exceeded 120 W m^{-2}[32]. The z_0 was estimated using Monin-Obukov Similarity Theory predictions of the mean horizontal wind speed under near-neutral conditions[52]. The analysis of turbulence measurements carried out at PM IGEO in 2013 yields average z_D and z_0 equal to 9.4m and 1.2 m, respectively.

Footprints of turbulence measurements in PM IAG, PM SFZ, PM ITU and PM IGEO were evaluated using Flux Footprint Prediction (FFP) model developed by Kljun et al.[65]. They were estimated considering observations carried out during two field campaigns in the MRSP (1st Campaign in February 19-28, 2013 and 4th Campaign in August 6-15, 2013) and one in the MRRJ (3rd Campaign in July 9-19, 2013). In the case of São Paulo, the FFP model was run using 30-minutes values of wind speed and direction, cross wind standard deviation, friction velocity and Obukhov length (L), every three hours to include UBL height estimated by Sánchez[111]. In the case of Rio de Janeiro (PM IGEO) UBL height (h) was estimated as: (a) 1500 m for $(z - z_D)/L < -0.05$; (b) $0.3\, u_*/|f|$ for $-0.05 < (z - z_D)/L < 0.05$, and (c) $0.3\sqrt{u_* L/|f|}$ for $(z - z_D)/L < 0.05$, where f is the Coriolis parameter and z is the turbulence measurements height. Two clipping approximations were assumed: (d) $h = 1500$ m when $h > 1500$ m during daytime and under neutral condition indicated by criteria (b); (e) $h = 400$ m during nighttime and under neutral condition indicated by criteria (b). It was assumed also that f in the expressions (b) and (c) are equal to one for latitude of 45°S (f = -1.0312 10^{-4} s^{-1}). This approximation was applied successfully to estimate PBL height at low latitudes like Rio de Janeiro by Oliveira et al.[92].

Original Research Article

As expected, the footprint indicated that the contribution area in each site increases as the measurement's height increases. For instance, during the 4th campaign around 90 % of turbulent fluxes measured at 9.6 m agl in PM ITU come from area within circle with radius of 300 m (yellow circle in Figure 6d). In the case of PM IAG only 60% of fluxes measured at 25.4 m agl come from an area within the circle with radius equal to 500 m (white circle in Figure 4f). And, in the case of PM SFZ only 30 % of the fluxes measured at 86.0 m agl come from area within with radius equal to 1 km (white circle in Figure 5e). For PM IGEO only 90 % of the fluxes measured at 22.7 m agl come from area within the circle of radius equal to 500 m (white circle Figure 6d) in the third campaign. In this case, the oceanic water surface at southwest may marginally contribute to the fluxes measured at PM IGEO during a small fraction of time as the wind flow from this sector (Figure 13d).

The geometric properties, given by the turbulence measurements height (25.4 m agl for PM IAG and 85.0 m agl for PM SFZ) and mean building heights (8.36 m for PM IAG and 19.75 m for PM SFZ) (Figure 7a), indicate that turbulence measurements carried in PM IAG and PM SFZ are performed 3 times in the case of PM IAG and 2.9 times the mean building height corresponding level in the inertial layer. On the other hand, in PM ITU the turbulence measurements are likely to be affected by the roughness sublayer of the forest canopy[106]. In the case of PM IGEO turbulence measurements height of 22.7 m agl and mean building height of 12.0 m (within 1-km radius circle) indicated that these measurements correspond to 1.9 times mean building height, indicating that they may be affected by roughness sub-layer effects.

According Fortuniak et al.[47] the systematic effects caused building can be mapped by analyzing vertical wind speed variance for near neutral conditions ($-0.01 < z/L < 0.01$). Figure 8d displays the normalized vertical wind speed standard deviation by u_* in terms of horizontal wind direction for turbulence measurements carried at the PM IAG from January 1st, 2013 to December 31st, 2014 for near neutral conditions. The normalized vertical wind speed standard deviation diverges from the empirical 1.25 (red line) proposed by Roth[108] for urban surface layer. Figure 8e display the sectors (shadow) where standard deviation deviated

more than one time its block average[47]. Turbulence data when the wind is blowing from these sectors are likely to be affected by building distortion therefore, they are removed from the data set. The criteria used to define objectively the sectors are more clearly indicated in the Figure 8f. The sectors are given by the deviation from the 1.25 normalized by $\sigma > 1.5$, where $\sigma = \sqrt{0.0049 + SE^2}$ and SE is the block standard error.

In this work 30-minutes values of H, LE, F_{CO2} and u_* are estimated for MRSP (PM IAG) during 1st (summer) and 4th (winter) campaigns (respectively February 19-28, 2013 and August 6-15, 2013) and for the MRRJ (PM IGEO) during 2nd (summer) and 3rd campaigns (respectively March 12-21, 2013 and July 9-19, 2013). Besides, SEB components: H, LE, G, R_N are estimated during 1st and 4th campaign in the MRSP for PM IAG (1st and 4th) and for PM ITU and PM SFZ (4th only). The anthropogenic heat (Q_F) is based on estimates by Ferreira et al.[41].

Surface wind pattern

Horizontal wind speed and direction are measured simultaneously with a sampling frequency of 0.5 Hz and store as 5-minutes averaged in all four platforms using 3-cup anemometer and vane model 034B MetOne Instruments Inc. (TABLE 2). These 5-minutes values are checked, and spurious values caused by malfunctioning and rain are removed. The resulting series are used to estimate monthly average hourly values considering the observation carried out from July 1st, 2013 to December 31st, 2014. More details about wind observation set ups can be found in TABLE A1 in the Appendix A.

Urban heat island

Urban heat island intensity is defined as the difference between the near-surface air temperature of urban (T_U) and non-urban (T_R) environments:

$$\Delta T = T_U - T_R \tag{7}$$

In midlatitude cities, the UHI intensity is highest during nighttime and in winter, with anthropogenic heat (house heating) playing the most important role[21,84,100]. The anthropogenic heat of tropical and subtropical cities is not as important as in other regions, there UHI are determined by solar heating (daytime maximum) and diurnal and seasonal patterns of soil moisture content[42].
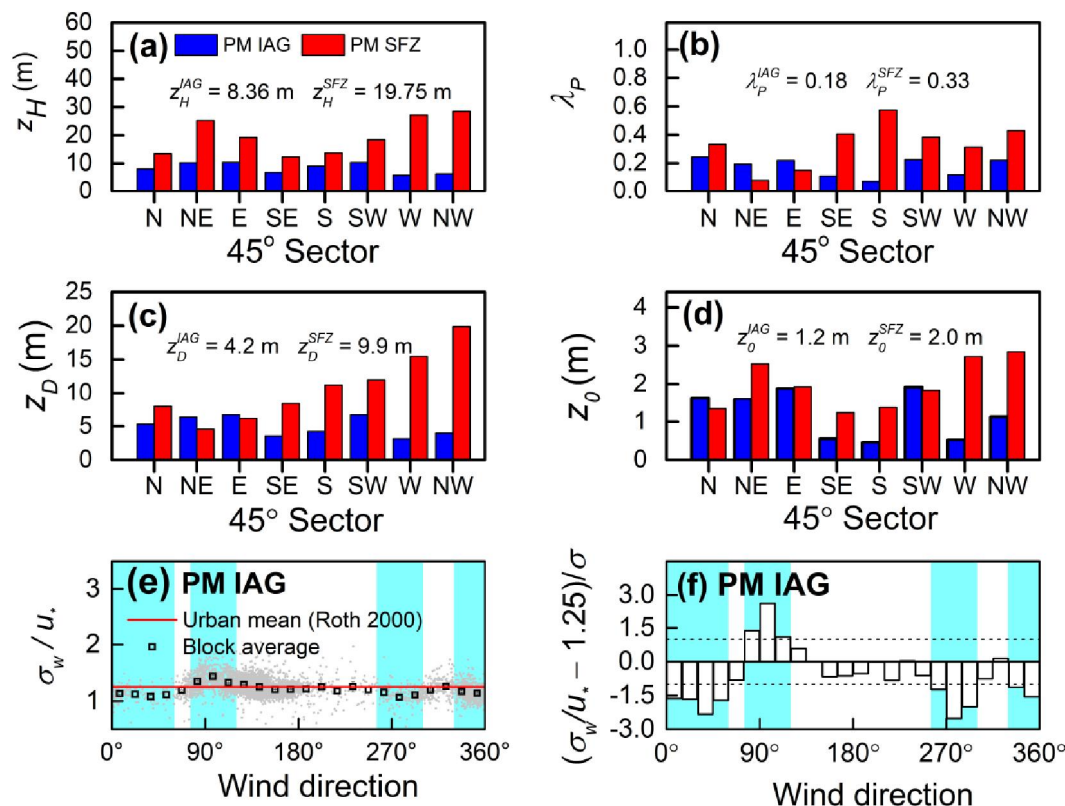
Original Research Article

Figure 7 : Radial distribution of (a) building height, (b) horizontal fraction of building area to total area (λ_p), (c) zero-plane displacement height (z_D), (d) roughness length (z_0); (e) dispersion diagram of vertical wind speed standard deviation (σ_w) in terms of horizontal wind direction, and (f) vertical wind speed normalized by its block average values in terms of horizontal wind direction. In (a)-(c) the 45° sector average was estimated in a 500-m-radius circle centered over the PM IAG (blue) and PM SFZ (red) indicated in Figures 4c and 5c respectively. In (f) $\sigma = \sqrt{0.0049 + SE^2}$, SE is the block standard error. (e) and (f) are based on turbulence measurements carried out from January 1st, 2013 to December 31st, 2014.

To estimate the UHI intensity in the MRSP, air temperature observations in the PM IAG at 18.7 m agl and PM SFZ at 78.6 m agl were used as a reference for suburban and urban areas, and air temperature observations in the PM ITU at 1.6 m agl were used as reference of rural area. For the MRRJ, air temperature observations in the PM IGEO at 17.2 m agl, INMET2 and INMET3 were used as a reference for suburban and urban areas, and INMET4 was used as reference of rural areas. Air temperature observations in the INMET sites in the MRRJ were carried out at 2.0 m agl. In the PM IAG, SFZ, ITU and IGEO air temperature measurements were carried by temperature and relative humidity sensors model CS219, Campbell Scientific Inc. In the INMET stations they are measured by a temperature and relative humidity sensors model QMH102, Vaisala. Details about set up of air temperature sensors in these sites are given in TABLE 2 and TABLE A1 in the Appendix A. In the platforms

air temperature were measured with a sample frequency of 0.5 Hz and stored as a 5-minute average and used to estimate hourly values, after quality control procedure that removes malfunction and rain effects. In the INMET2-4 sites hourly values are obtained from INMET[61]. After quality control procedure, all hourly values of air temperature are extrapolated linearly to 1.5 m agl using dry air lapse rate. In this work, the UHI intensity is evaluated considering hourly values of air temperature at 1.5 m agl observed in the MRSP (PM IAG, PM ITU, PM SFZ) and in the MRSP (PM IGEO, INMET2, INMET3, INMET4) from July 1, 2013 to December 31st, 2014.

Urban boundary layer

During daytime UBL height is estimated using two methods: air temperature gradient method for rawinsonde data[112] and Wavelet Covariance Transform Method (WCT) for lidar data[11,51]. In the air temperature gradient method, the UBL height is given

by the level where the vertical gradient of temperature becomes positive or equals to zero by the first time. Under stable conditions the air temperature gradient is adapted to identify the top of the surface temperature inversion layer. The WCT method was applied to identify the UBL height during the convective daytime period only. In this condition the UBL top is detected by an abrupt change in the function $(W(a, b))$, which is obtained from the covariance between a mother wavelet function and the normalized Range Corrected Signal (*RSC*) provided by the lidar system. So that, the UBL height is the value of b corresponding to first maximum of $W(a, b)$. The equation below describes the $W(a, b)$:

$$W(a,b) = \frac{1}{a} \int_{z_b}^{z_t} RCS(z)HA\left(\frac{z-b}{a}\right) dz \quad \textbf{(8)}$$

where: *HA* is the Haar function (the mother wavelet), z_b and z_t are the bottom and upper limits, respectively, of the backscattered signal, a is the dilatation related to the extent of the step function and b is the translation, or in other words, the location of the step. The *RSC* profile used in $W(a, b)$ is composed by the average of 10 profiles. Details about the Lidar characteristics and WTC method can be found in Landulfo et al.[70], Mariano et al.[79] and Granados-Munoz et al.[51]. The lidar used in both MRSP and MRRJ is a MSP-2 lidar is a biaxial system, which operates with a pulsed Nd:YAG laser emitting in the wavelength 532 nm. Such system operates in the elastic channel 532 nm and in the Raman-shifted channel 607 (from N_2). The MSP-2 full overlap is reached around 180 m asl. This system was operated with a spatial and temporal resolution of 7.5 m and 1 min, respectively. This system is part of Latin American Lidar Network (LALINET)[6]. In this work UBL and surface inversion layer thickness were estimated for: February 20, 2013, July 12, 2013 and August 8, 2013, corresponding to 1st (summer, MRSP), 2nd (winter, MRRJ) and 4th (winter, MRSP) field campaigns.

Climate

Using the Koppen classification Alvares et al.[3] combined all data available at the surface, including the data used here (TABLE A2, Appendix A), came up with two predominant distinct climates for the metropolitan areas of São Paulo and Rio de Janeiro: Cwb (Humid subtropical with dry winter and temperate summer) for the MRSP and Aw (Tropical with dry winter) for the MRRJ. However, the climate in these two regions does not show such dramatic differences. Both areas are characterized by a warm and wet summer and a mild cold and dry winter (Figure 8). Despite the similar latitude (Figure 1), the MRSP is located at a much higher altitude (~750-800 m asl) and at approximately 60 km far from the Atlantic Ocean. Consequently, in average São Paulo is approximately 4.6° C colder there than Rio de Janeiro (Figure 8a). Similarly, compared to the MRRJ the relative humidity is higher in MRSP, mainly in the southern portions (as indicated by PEFI in Figure 8b). In general, this happens because in the MRSP precipitation is higher (Figure 8c) and temperature is lower Figure 8a). Another important factor is the sea-breeze circulation[94,125]. Sea breeze penetrates in São Paulo systematically after noon time, cooling and wetting the region[104].

In general, the wind speeds are lower in both regions during the dry season (minimum of 1.7 ms^{-1} in May in southern MRSP (PEFI) and 1.9 ms^{-1} in June in MRRJ (INMET1)) and are higher during the wet season (maximum of 3.1 ms^{-1} in November in northern MRSP (MIRANTE)) (Figure 8d). Comparatively in the MRSP, the surface wind is systematically lower in the south (PEFI). The surface wind in both metropolitan regions show similar seasonal patterns associated with a combination of large-scale systems that are disrupted by transient modifications such as synoptic scale disturbances[30] and by mesoscale and local circulations associated with topography and land use features in these two regions[94,98,104].

PRELIMINARY RESULTS

This section will focus on the observational characterization of the following features: surface radiation balance; surface energy balance and turbulent fluxes; surface wind pattern; UHI; and urban boundary layer. Monthly average values, mainly February and August of SRB components, surface wind and UHI described here correspond to observations carried out
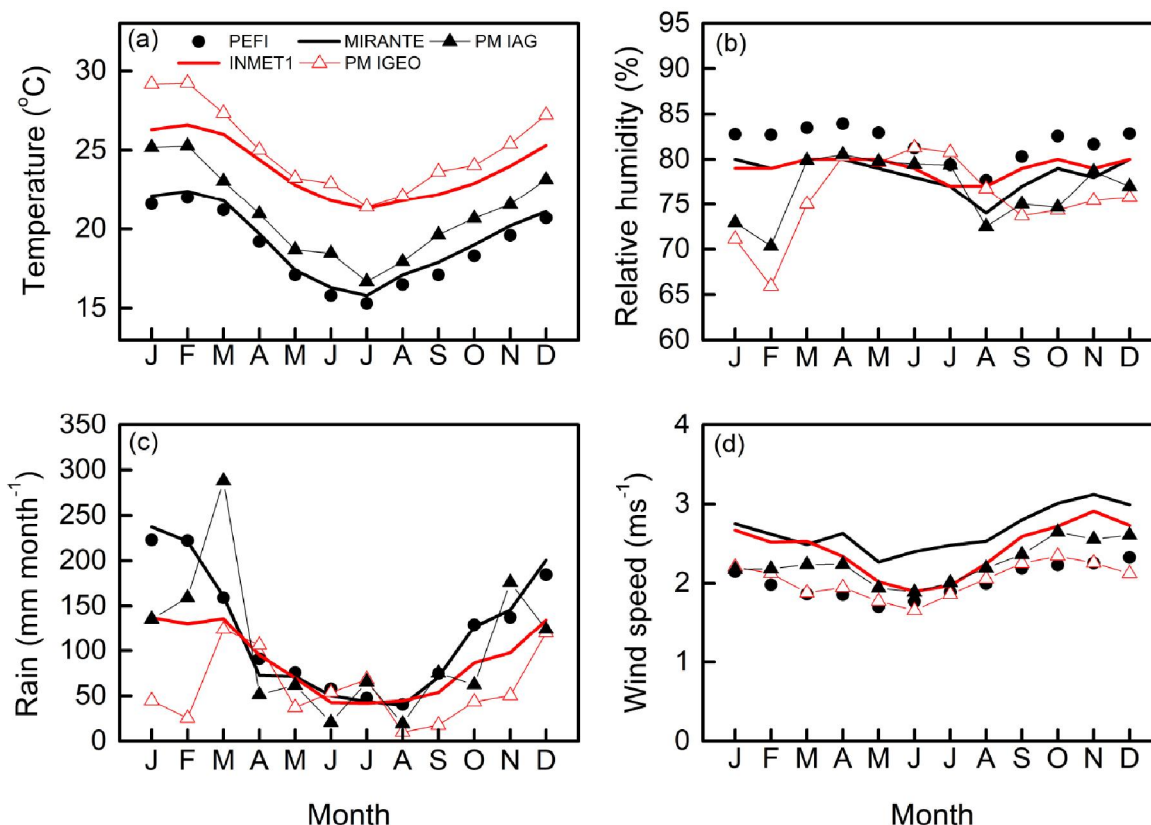
Original Research Article

Figure 8 : Seasonal variation of monthly average values of (a) air temperature, (b) relative humidity, (c) rain and (d) wind speed in the MRSP and MRRJ. The periods of observation are indicated in TABLE A2 in the Appendix A.

between July 1, 2013 and December 31, 2014. According to Ferreira et al.[42] and Marques Filho et al.[81] February and August are considered representative of summer and winter for both metropolitan regions.

Surface radiation balance

The diurnal evolutions of all SRB components (monthly average hourly values) observed in the MRSP, at PM IAG, ITU and SFZ and in the MRRJ at PM IGEO during February and August are indicated in Figure 9 and TABLE 3. There, negative (positive) irradiances indicate downward (upward) energy fluxes.

The magnitudes of the diurnal evolution of SW_{DW} in the MRRJ in both February and August are higher than the SW_{DW} magnitude in any platform in the MRSP. This is not the case for SW_{UP}, which shows the highest magnitudes in the PM SFZ and the lowest in PM ITU in both February and August in the MRSP. The SW_{TOP} magnitudes for the MRRJ in February and August are slightly higher than those for the MRSP in February and August (Figure 9a-b, TABLE 3). Larger SW_{DW} values in the MRRJ with respect to the MRSP can be explained

in terms of the differences in the seasonal variation of cloud activity in these metropolitan regions[81,93]. Since it rains more in the RMSP in both February and August (Figure 8c), it seems reasonable to infer that attenuation of solar radiation by clouds is greater in the MRSP. High pollution levels[5], mainly in winter months, may also contributed to lower SW_{DW} magnitude in the MRSP comparatively to MRRJ. Indeed, according to Codato et al.[26] the MRSP displays SW_{DW} reduction up to 7.8 % compared to not-urban areas. Air pollution effects can also explain the local variability observed in the MRSP, where observations in PM ITU (rural) display the largest SW_{DW} and PM SFZ (urban) displays the smallest one (TABLE 3).

The magnitudes of the diurnal LW_{DW} and LW_{UP} cycles in the MRRJ in February and August are higher than the magnitudes on any platform in the MRSP (Figure 9c-9d, TABLE 3). These differences in the magnitude of LW_{DW} occur mainly because the air temperature in the MRRJ is systematically higher (~4.6°C) than in the MRSP during all months of the year (Figure 8a). This behavior reflects also the larger
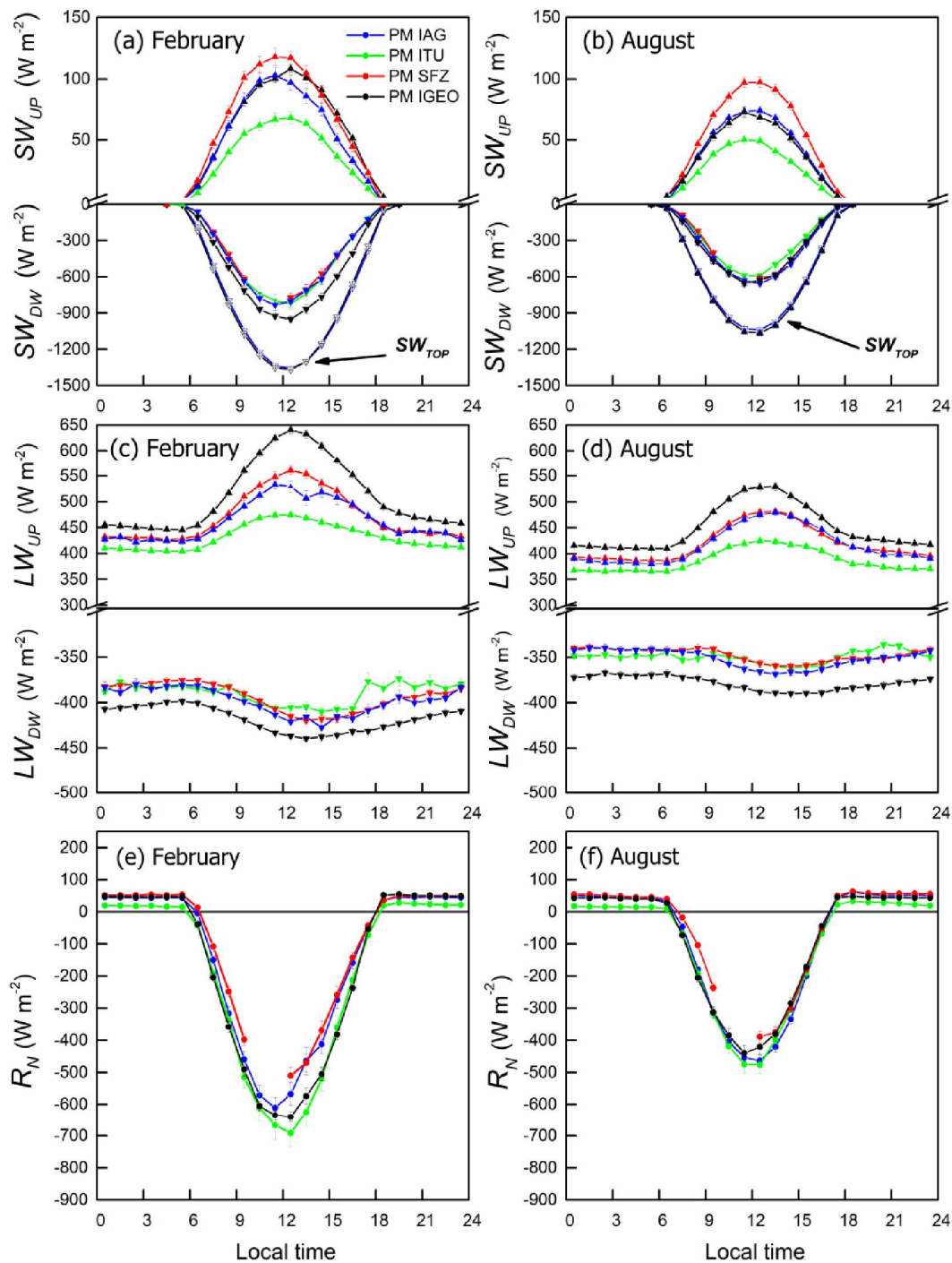
Figure 9 : Diurnal evolution of the monthly average hourly values of SRB components in the PM IAG (blue), PM ITU (green), PM SFZ (red) and PM IGEO (black) during February and August (TABLE 3). Vertical bars correspond to statistical errors ($\sqrt{\sigma^2/N}$), where σ is the standard deviation and N is the number of values. Negative (positive) irradiances indicate downward (upward) energy fluxes. Observations carried out from July 1st, 2013 to December 31st, 2014.

input of SW_{DW} in the MRRJ discussed above and fact that MRSP is located 60 km far from the shoreline and about 700 m asl. Within the MRSP, the smallest magnitude of the diurnal evolution of LW_{DW} and LW_{UP} are observed at the PM ITU in both February and August. This is a consequence of the fact that the PM ITU is in a rural area where air temperature is systematically smaller due to the UHI effect (see section Urban heat island).

As expected from the discussion above, the

Original Research Article

magnitudes of R_N in the MRRJ in February and August are larger than the magnitudes of any platform located in urban (PM SFZ) and suburban (PM IAG) areas in the MRSP, where the largest R_N is observed in the PM ITU (daytime) and smallest in the PM SFZ (daytime) (Figure 9e-9f). Therefore, there is more energy available to be transferred to the atmosphere as sensible and latent heat and to be stored in the canopy in the MRRJ than in the MRSP. The consequences of this will be analyzed in the subsequent subsections.

Within the MRSP, there are significant differences in all SRB components. These differences reflect the spatial variation of the land use. For instance, at the PM ITU (rural land use), the daytime the magnitude of R_N is systematically larger than in the urban and suburban areas. This happens because R_N in PM ITU closely follows SW_{DW} since the albedo is small (0.085±0.004) compared to the PM IAG (0.121±0.004) and the PM SFZ (0.162±0.007).

During nighttime periods the magnitude of R_N in rural area (PM ITU) is systematically smaller than in urban and suburban of the MRSP. In general, the albedo in urban areas located at middle latitude is smaller than adjacent rural areas due to a combination of geometric and material effects[42,90]. On the other hand, lower albedo of forest canopy is also commonly observed at midlatitudes regions in the absence of snow[20]. The albedo in TABLE 3 corresponds to the mean ratio of monthly average hourly values of SW_{UP} and SW_{DW} observed between 09:30 and 15:30 LT. Curiously, the albedo at the PM IAG (0.121±0.004) is similar to that at the PM IGEO (0.114+0.004). In this case, both platforms have similar radiometric characteristics, once they are located on the top of buildings with a similar geometry and roof fabric (Figure 2a,d). No significant seasonal variations in the albedo measured at the PM IGEO (~2%). On the other hand, the albedo varied ~6% for the PM IAG (TABLE 3).

TABLE 3 : Seasonal variation of the diurnal magnitude for SRB components (SW_{DW}, SW_{UP}, LW_{DW}, LW_{UP}, R_N), shortwave downward at the top of the atmosphere (SW_{TOP}) and albedo in the MRSP and MRRJ. Negative (positive) irradiances (W m⁻²) indicate downward (upward) energy fluxes. Observations carried out from July 1ˢᵗ, 2013 to December 31ˢᵗ, 2014.

Radiation variables	February			
	PM IAG (LCZ 6)	PM ITU (LCZ A)	PM SFZ (LCZ 8)	PM IGEO (LCZ 6)
SW_{DW}	-833±46	-822±52	-773±36	-952±24
SW_{UP}	103.0±5.9	68.5±4.5	118.0±7.1	108.3±2.9
LW_{DW}	-427.5±3.0	-410.1±3.9	-419.7±2.3	-439.8±2.3
LW_{UP}	532.8±7.9	474.8±5.2	560.8±7.8	640.3±6.7
R_N*	-611±33	-692±42	-484±31	-640±16
	47.0±4.2	28.2±3.8	54.2±3.3	54.9±2.2
	658±94	720±140	538±67	695±45
SW_{TOP}		-1335.10±0.65		-1369.7±3.1
Albedo	0.124±0.002	0.085±0.001	0.160±0.004	0.115±0.002
Radiation variables	August			
	PM IAG (LCZ 6)	PM ITU (LCZ A)	PM SFZ (LCZ 8)	PM IGEO (LCZ 6)
SW_{DW}	-658±28	-592±35	-610±27	-654±37
SW_{UP}	74.4±3.5	50.1±3.1	97.5±4.3	73.1±4.3
LW_{DW}	-368.6±3.1	-362.3±3.1	-359.7±2.8	-390.0±2.3
LW_{UP}	479.3±5.5	424.6±5.2	481.8±5.3	529.4±7.2
R_N*	-464±21	-476±28	-389±17	-440±25
	60.8±3.7	33.0±3.6	63.5±3.6	48.5±3.4
	525±56	509±86	453±46	489±62
SW_{TOP}		-1039.8±1.5		-1067.6±4.1
Albedo	0.117±0.002	0.085±0.002	0.164±0.003	0.112±0.002

(*) **Daytime minimum, nighttime maximum and magnitude (nighttime maximum minus daytime minimum).**

Original Research Article

Differently from higher latitude cities, suburban areas in the MRSP and MRRJ do not display large seasonal variability associated to vegetation effect[42].

Surface energy budget and turbulent fluxes

The diurnal evolutions of H, LE, F_{CO2} and u_* based on 10-days average hourly values observed in the suburban area of the MRSP (PM IAG, LCZ 6) during 1st (summer) and 4th (winter) campaigns (respectively February 19-28, 2013 and August 6-15, 2013) and of the MRRJ (PM IGEO, LCZ 6) during 2nd (summer) and 3rd campaigns (respectively March 12-21, 2013

and July 9-19, 2013) of the MCITY Brazil project are indicated in the Figure 10. There, positive (negative) H, LE and F_{CO2} fluxes indicate upward (downward) energy and mass fluxes.

During the summer campaigns (1st and 2nd), the magnitudes of H and LE at the PM IAG (February) (Figure 10a,e) were larger than those at the PM IGEO (March) (Figure 10b,f). This was unexpected because, as discussed in previous section, the magnitude of the net radiation in the PM IGEO is larger than those observed in the PM IAG during summer (Figure 9e). One possible explanation for this discrepancy is that
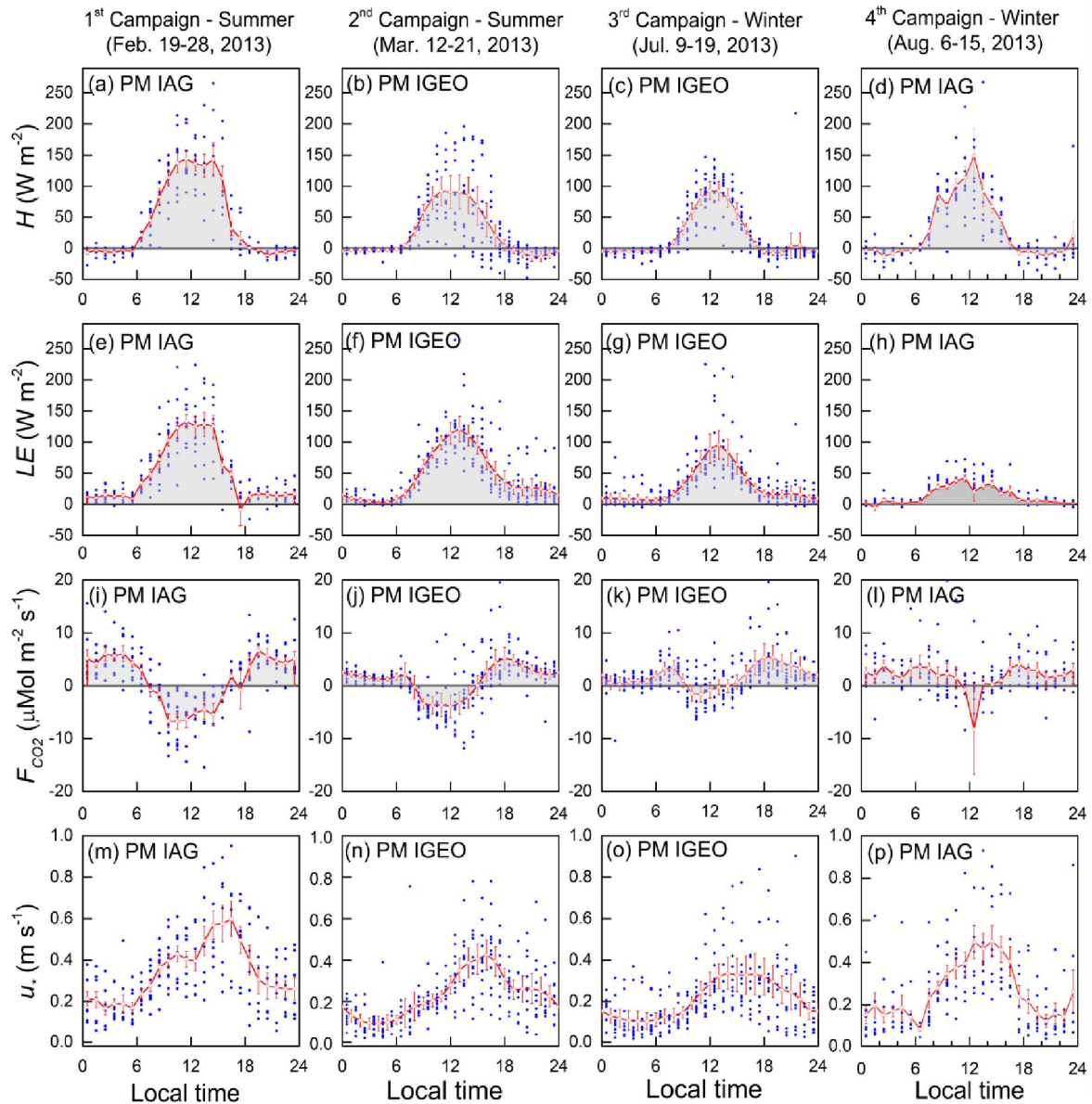

Figure 10 : Diurnal evolution of turbulent vertical fluxes of (a)-(d) sensible heat, (e)-(h) latent heat, (i)-(l) CO_2 and (m)-(p) friction velocity observed during field campaigns in the MRSP (PM IAG) and MRRJ (PM IGEO). Red continuous lines indicate mean values, blue solid circles hourly values, and vertical bars the statistical error of the mean.

Original Research Article

during the 2nd campaign in the MRRJ (March), the South Atlantic Convergence Zone was inducing heavy precipitation in Rio de Janeiro during the second half of March (Figure 8c). This anomalous precipitation may have altered the summer pattern of clouds in the MRRJ, reducing the R_N and, consequently, the magnitude of H and LE.

During the winter campaigns (3rd and 4th), the magnitude of H in the PM IGEO in July (Figure 10c) was smaller than that at the PM IAG in August (Figure 10d). On the other hand, the magnitude of LE at the PM IGEO (Figure 10g) was larger than that at the PM IAG (Figure 10h). August is the driest month of the year in the MRSP (Figure 8b), so there is less moisture available to evaporate at the surface, justifying the small LE observed at the PM IAG. On the other hand, the PM IGEO in July is wetter than that at the PM IAG. Another possibility is the contribution of Guanabara Bay to evaporation during winter; both wind roses indicated a significant fraction of the time the winds in PM IGEO are from ENE and E (Figure 13d).

The F_{CO2} magnitude is larger at the PM IAG (Figure 10i) compared to the PM IGEO during the summer campaigns (Figure 10j). In both metropolitan regions, the diurnal cycles indicate a positive CO_2 flux (emission) during nighttime associated with local vegetation respiration and a negative CO_2 flux (reduction) during daytime associated with photosynthesis. This diurnal pattern indicates that local vegetation plays an important role in the CO_2 in both areas, as expected for suburban areas[28]. For the winter campaigns, the F_{CO2} magnitudes are smaller in both regions and indicate much less daytime depletion by photosynthesis (Figure 10k-l). According to Cotovicz Jr et al.[27], there are indications that *Guanabara* Bay is affecting CO_2 behavior at *Fundão* Island. Footprint analysis (Figure 6d) indicated that a portion of the bay water is located within the 90%-contour line area at west of PM IGEO. The both F_{CO2} peaks early in the morning and evening in the PM IGEO and PM IAG correspond to the rush hours from vehicular emissions in these suburban areas. The net daily CO_2 flux for PM IAG and PM IGEO during summer campaigns are 3.27 kg m^{-2} day^{-1} and 3.56 kg m^{-2} day^{-1}, respectively. During the winter campaigns

the net daily CO_2 flux almost double with 6.17 kg m^{-2}day^{-1} and 6.65 kg m^{-2} day^{-1} in PM IAG and PM IGEO, respectively. According to Velasco and Roth[124] these values are consistent, but smaller than the ones expected for suburban areas with vegetation fraction between 25% and 33% like PM IAG and PM IGEO (TABLE C1 Appendix C).

The time evolution of u_* during the field campaigns (Figure 10m-p) indicates a diurnal pattern with a daytime maximum and nighttime minimum. The friction velocity magnitude is larger in the MRSP and during the summer campaign. This behavior can be explained by the seasonal variation of the wind speed (Figure 13a-b). The daytime maximum wind speed magnitude during summer months are produced by the intensification of both sea-breeze circulation and downward turbulent flux of momentum in the convective PBL during summer months.

The major features observed in the mean diurnal evolution of H and LE (Figure 10) can be better identified by comparing the mean daily values (integrated over a 24-hour period) of H and LE in TABLE 4. A Bowen ratio value above 1 during winter in the PM IAG indicated that in São Paulo ground is drier than in Rio de Janeiro. Besides, the presence of large portions of water may contribute the increase LE in the PM IGEO site. During summer, LE is larger than H because the ground is wetter in both metropolitan regions so the contributions of evapotranspiration of blowing local vegetation are larger[43].

Figure 11 displays the diurnal evolution of the Bowen ratio and ratios of sensible and latent heat fluxes to the net radiation (sign changed) observed in the MRSP and MRRJ during summer and winter campaigns of 2013. The behavior all three ratios display similarities to the results obtained by Ferreira et al.[43] for PM IAG. Bowen ratio is negative during nighttime and positive during daytime (Figure 11a-d) in all four cases, but high magnitudes (greater than 2) like observed by Ferreira et al.[43] were obtained only in the 4th campaign in the PM IAG when RMSP is very dry. The upward spikes observed in the both ratios $H/-R_N$ and $LE/-R_N$ (Figure 11e-h) indicated that both H and LE remain small but positive when R_N passing through zero in PM IGEO in 2nd and 3rd campaigns.

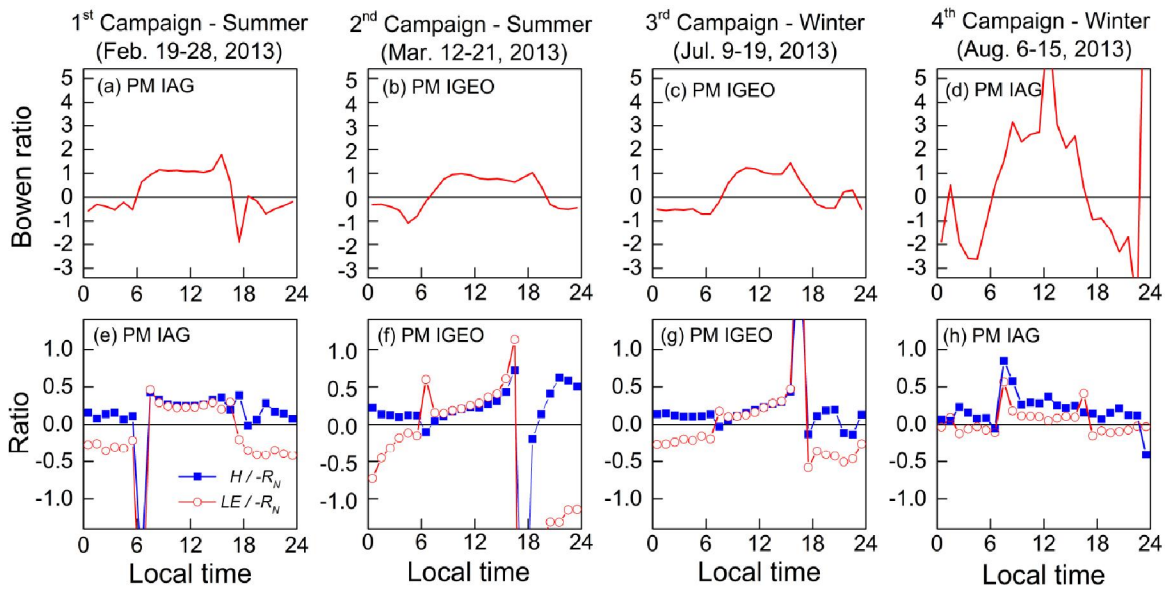# Original Research Article

Figure 11 : Diurnal evolution of (a)-(d) Bowen ratio and (e)-(h) ratio of sensible heat and latent heat fluxes to the net radiation. Mean hourly values observed during the field campaigns in 2013 in the MRSP (PM IAG) and RMRJ (PM IGEO).

TABLE 4 : Mean daily values of H and LE, Bowen ratio and daytime and nighttime ratio of H and LE to -Rn measured at the PM IAG (LCZ 6) and PM IGEO (LCZ 6) during 10-day field campaigns in 2013.

SEB (MJ m^{-2} day^{-1})	Campaign (daily values)			
	1st (Feb. 19-28) (MRSP) PM IAG	2nd (Mar. 12-21) (MRRJ) PM IGEO	3rd (Jul. 9-19) (MRRJ) PM IGEO	4th (Aug. 6-15) (MRSP) PM IAG
H	3.87±0.36	2.10±1.74	1.78±0.82	2.33±0.31
LE	4.30±0.03	3.93±1.09	2.64±1.29	1.10±0.17
Bowen	0.90±0.09	0.62±0.57	0.83±0.49	2.12±0.61
Daytime (08:00-16:00 LT)				
Ratio	1st	2nd	3rd	4th
Bowen	1.10±0.01	0.83±0.04	1.05±0.09	3.24±0.62
$H/-R_N$	0.29±0.02	0.25±0.03	0.22±0.04	0.31±0.04
$LE/-R_N$	0.25±0.01	0.31±0.05	0.22±0.05	0.11±0.01
Nighttime (00:00-04:00 LT and 20:00-24:00 LT)				
Ratio	1st	2nd	3rd	4th
Bowen	-0.44±0.06	-0.41±0.03	-0.32±0.13	-2.10±0.60
$H/-R_N$	0.15±0.02	0.34±0.08	0.07±0.04	0.07±0.07
$LE/-R_N$	-0.34±0.02	-0.82±0.16	-0.33±0.04	-0.04±0.02

TABLE 4 shows that the mean Bowen ratio, mean daily values of H and LE ratio, varied from 0.90±0.09 (1st) to 2.12±0.61 (4th) in the PM IAG in the MRSP, and from 0.62±0.57 (2nd) to 0.83±0.49 (3rd) in PM IGEO in the MRRJ. Considering that all three ratios change sign during the day-night transitions (Figure 11a-d), it is convenient to split their average values into daytime and nighttime values (TABLE 4). Daytime values of Bowen ratio in PM IAG during 1st (1.10±0.01) and in PM IGEO during 2nd (0.83±0.04) and 3rd (1.05±0.09) campaigns are smaller than 1.57, observed by Ferreira et al.[43] from May 18 and June 17 of 2009 in the PM IAG. These values differ also from typical Bowen ratio values observed in midlatitudes cities (1.27-9.85)[43]. Only in the 4th campaign in PM IAG and IGEO the Bowen ratio displayed values comparable to observed previously in São Paulo and within interval of values expected for suburban areas in midlatitudes cities[43]. The other ratios ($H/-R_N$ and $LE/-R_N$) are very similar to the ones obtained by Ferreira et al.[43]. This indicated that partition of R_N between H and LE in both PM IAG and PM IGEO are consistent with expected for suburban areas.

The diurnal evolution of the SEB components during the 1st Campaign (February 19-28, 2013) and the 4th Campaign (August 6-15, 2013) in the MRSP are indicated in Figure 12. During the summer campaign of February, only the PM IAG was set up in São Paulo. During the winter campaign of August, all three platforms (PM IAG, PM ITU, PM SFZ) were working. In the summer campaign LE and H are similar, indicating a Bowen ratio on the order of 1. During the winter campaign the magnitude of LE is lower than H, and the Bowen ratio is greater than 1. The residue - estimated as: $R_N + Q_F - (H + LE + G)$, where G is the soil heat

Original Research Article

measured only in the PM IAG and PM ITU -is assumed as an indication of stored heat flux in the canopy. Heat flux to the buildings was not measured in both urban and suburban sites. The anthropogenic heat estimated by Ferreira et al.[41] for the City of São Paulo was used in the SEB of the urban (PM SFZ) and suburban (PM IAG) sites. As indicated in Figure 12, the inclusion of Q_F (magnitude ~ 20 W m^{-2}), does not affect significantly the SEB in both sites. Similarly, G in PM IAG and PM ITU correspond to a small fraction of SEB in these sites. During the winter campaign the residue in the rural site (PM ITU) is smaller than in the suburban (PM IAG) and urban (PM SFZ) sites. In the rural site the residue displays a maximum in the morning indicating the stored energy flux there is used to heat the forest biomass. Due to a denser distribution of taller buildings (Figure 5), the magnitude of the stored energy flux is largest in the urban site (PM SFZ).

Surface wind pattern

Figure 13 displays the wind roses for the PM IAG, ITU, SFZ and IGEO. In the case of São Paulo, the frequency distribution of the wind speed and direction observed in the PM IAG and PM SFZ are similar, with the most frequent direction from the SE. In the PM ITU, the most frequent wind direction is east. The SE wind in São Paulo indicates the presence of sea-breeze circulation shifting the wind direction at the surface from NE to SE and the passage of cold fronts shifting the wind direction at the surface from NW to SE[94,125]. In the case of the PM ITU, the wind intensity is much lower because in this site measurements were performed about 2.5 m above the mean forest canopy height. As result of this proximity with forest canopy top direction changes associated with sea-breeze are less pronounced than in the other sites in the MRSP. Besides, at this platform, the winds may be under the influence of local
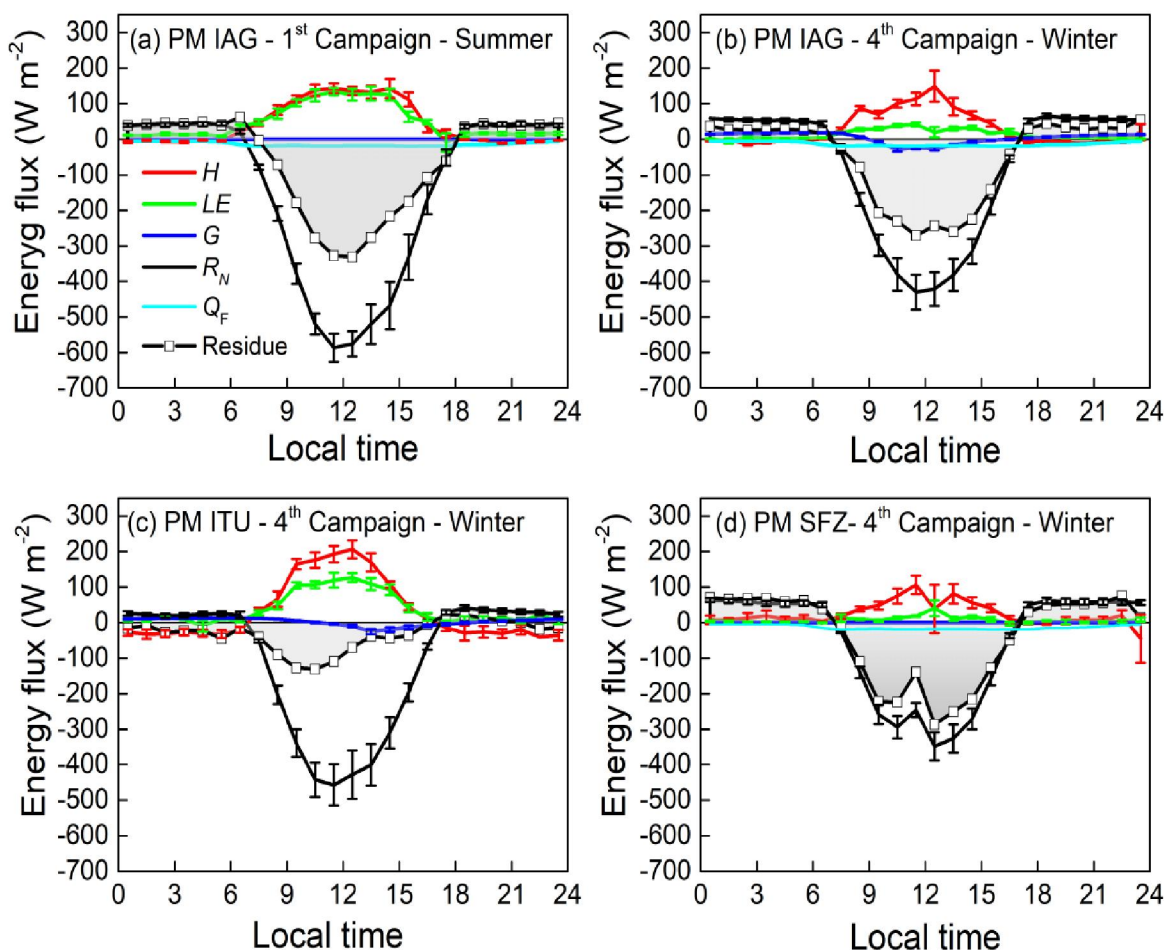

Figure 12 : Diurnal evolution of mean values of the SEB components observed during the 1st Campaign in the MRSP at (a) the PM IAG (February 19-28, 2013) and the 4th Campaign (August 6-15, 2013) in the MRSP at (b) the PM IAG, (c) the PM ITU and (d) the PM SFZ. Vertical bars correspond to the statistical error of the mean.
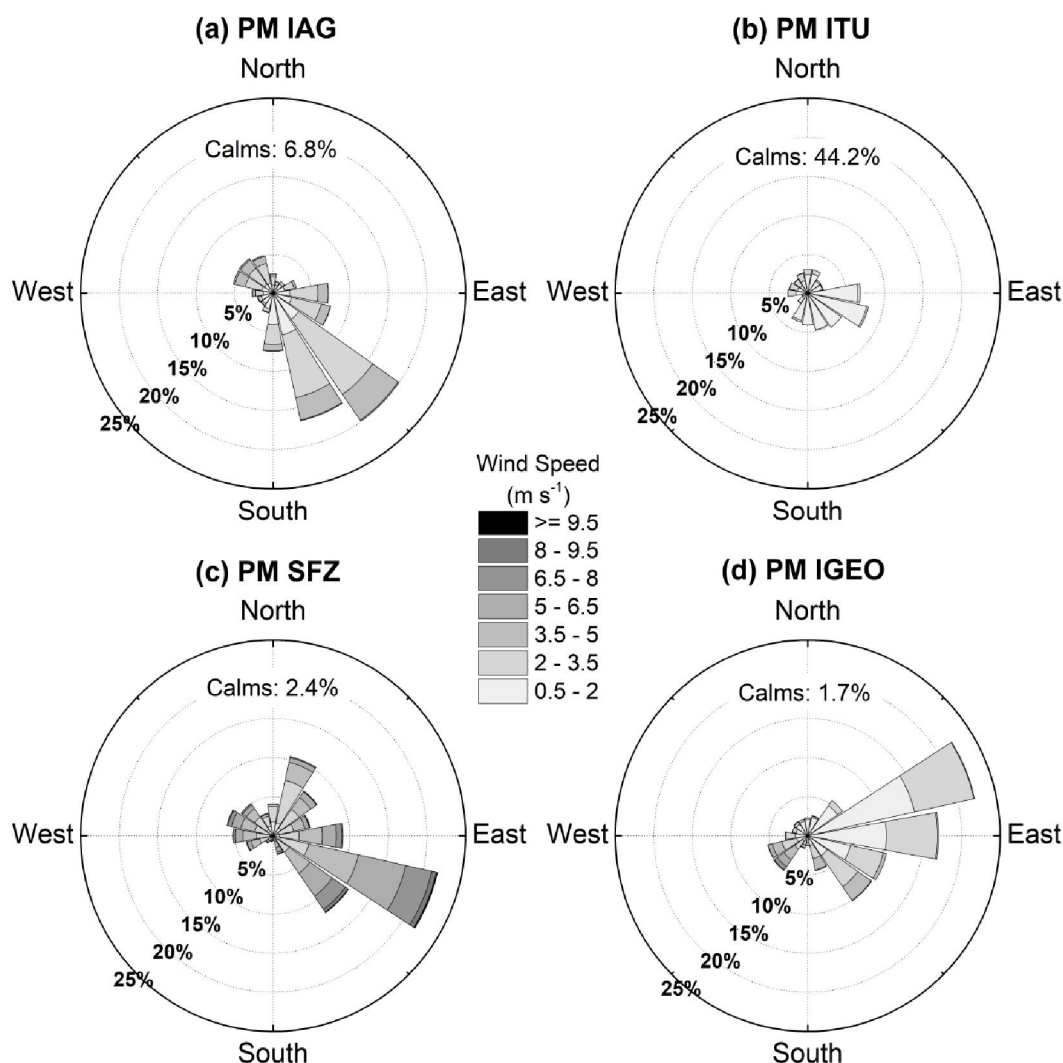
Figure 13 : Wind roses for (a) PM IAG, (b) PM ITU, (c) PM SFZ and (d) PM IGEO. Based up on measurements carried out by 3-cup anemometer and vane from July 1st, 2013 to December 31st, 2014 (TABLE 2 and TABLE A1 in the Appendix A).

circulations associated with the large water body (Billings Dam) located at the north and UHI circulation. This local circulation is likely to induce a NW wind that may be offset by a stronger SE flow from sea breeze. In the case of Rio de Janeiro (Figure 13d), the highest frequency wind direction is from the ENE and is associated with a combination of large-scale NE flow (section Climate), sea-breeze circulation (from *Guanabara* Bay at east, Figure 1d) and blocking effects induced by a chain of cliffs and mountains at the south (Figure 1f). The sea-breeze circulation from the Atlantic Ocean is less frequent in the PM IGEO than the sea breeze from Guanabara Bay because of blocking effects, but it contributes to a secondary maximum of the frequency in the SE direction (Figure 13d). Urban and other land-use effects are unclear in these wind roses.

The diurnal evolutions of monthly average wind speed and direction are indicated in Figure 14 for February (summer) and August (winter) in the MRSP and MRRJ. There, one can see that the wind speed in the PM SFZ (measured at 85 m agl) has the largest magnitude in February (Figure 14a), varying from 2.5 ± 0.2 m s^{-1} during nighttime (03:30 LT) to 6.4 ± 0.3 m s^{-1} by the end of the afternoon (16:30 LT). The wind speed at the PM ITU (measured at 9.7 m agl) displays the smallest magnitude, varying from 0.20 ± 0.07 m s^{-1} during nighttime (02:30 LT) to 1.7 ± 0.1 m s^{-1} around noon (11:30 LT). The wind speed at the PM IAG (measured at 26.5 m agl) shows an intermediate magnitude varying from 1.1 ± 0.1 m s^{-1} during nighttime (02:30 LT) to 3.6 ± 0.2 m s^{-1} in the afternoon (16:30 LT). In August, the nighttime wind speed in all platforms

Original Research Article

are greater than that in February and the daytime wind speed are smaller. In both months, the wind speed displays a maximum intensity in the middle of the day (Figure 14a,b) in the PM ITU. In the PM IAG and PM SFZ, the wind speed displays a minimum during the night-to-day transition and a maximum between 15:00 and 18:00 LT.

The diurnal evolution of the wind direction in all three platforms shifts anti-clockwise from E-NE to SE from mid-morning to mid-afternoon (Figure 14c,d) in association with the sea breeze penetration into São Paulo[94]. In the PM IGEO, the daytime maximum of 3 m s^{-1} occurs between 15:00 and 16:00 LT and is associated with the wind direction from the SE quadrant, indicating sea breeze intensification during the afternoon. This pattern is clearer in February than August. In August, the nighttime winds from W are associated with the intensification of the land-breeze at the PM ITU and PM IGEO (Figure 14d). In February, the nighttime thermal contrasts associated with land-breeze were not observed at either metropolitan region. Winds from the S-SE sectors are an indication that post-frontal anticyclonic circulation is a frequent feature of both metropolitan regions[31,94,125].

It is important to emphasize that correction for over speeding effects were not carried out here. Unfortunately, we could not find any empirical correction for over speeding and other similar building effects in the literature. However, according to Giometto et al.[49] buildings with flat roof, as used here (Figure 2a,c,d), display minimal over speeding effect, so it can be assumed that wind speed measurements used here are not substantially affected. On the other hand, according to Oke[91], these effects can only be taken into consideration properly by performing wind tunnel experiment and CFD numerical simulations, taking into consideration the building geometry. The analysis of these effects is underway, and the results will be addressed in a near future publication.

Urban heat island

The seasonal variation of the UHI intensity in the MRSP and MRRJ are shown in the Figure 15. In both metropolitan regions, a general pattern arises with a daytime minimum alternated by nighttime maximum.

In the MRSP both estimates (Figure 15a,b) indicate a similar pattern with daytime positive minimum (09:00 and 13:00 LT) and maximum (14:00 and 17:00 LT). In
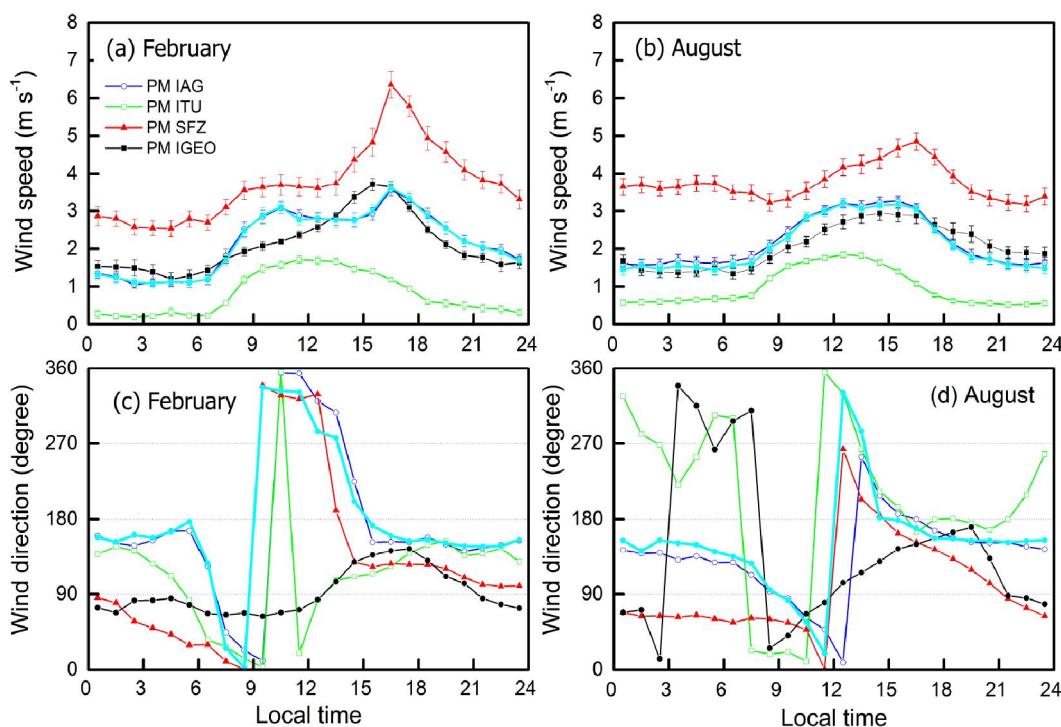

Figure 14 : Seasonal evolution of the wind speed and direction at the PM IAG (blue line), PM ITU (green line), PM SFZ (red line) and PM IGEO (black) during February and August. Observations carried out from July 1st, 2013 to December 31st, 2014.
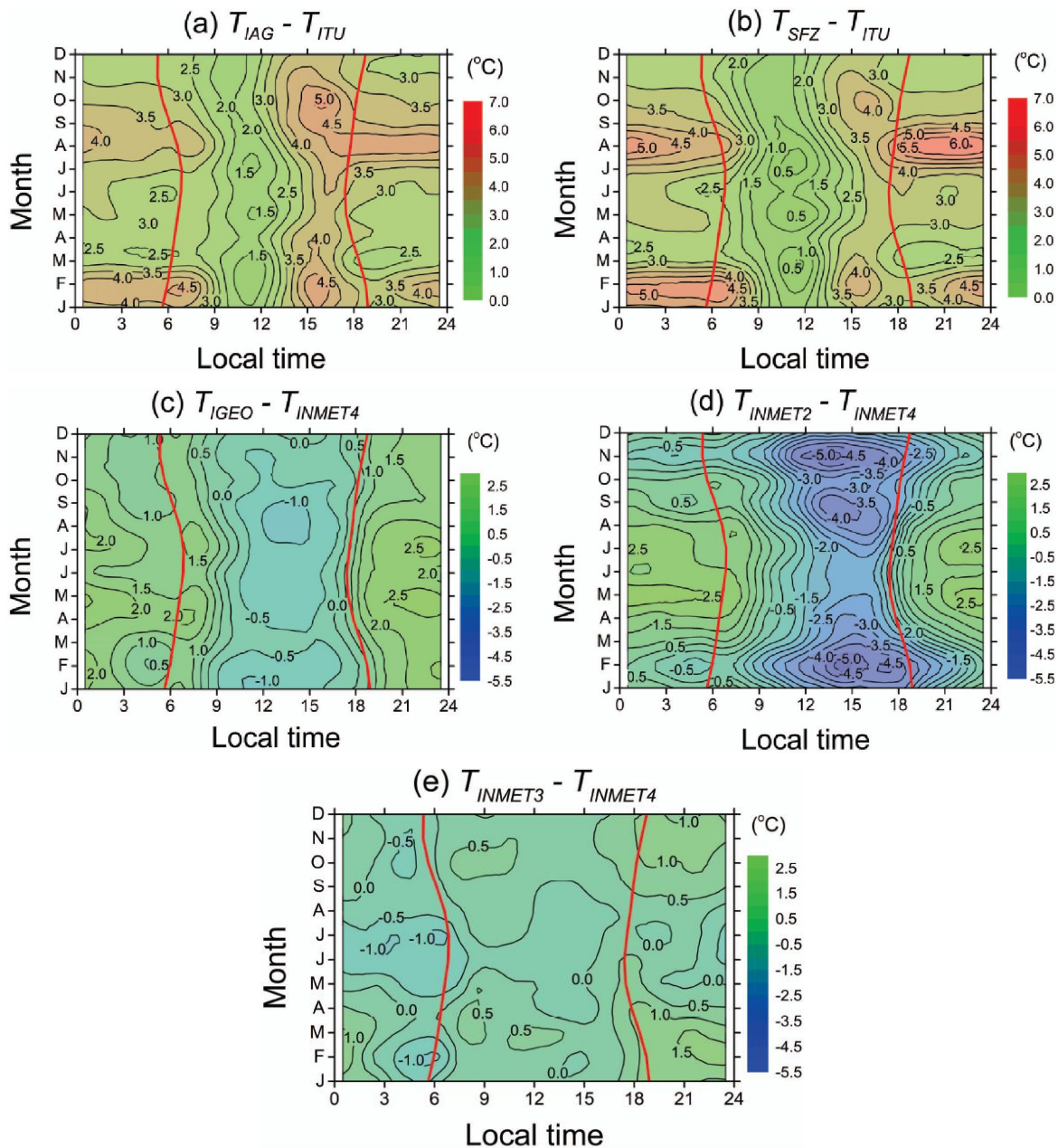
Original Research Article

Figure 15 : Diurnal evolution of the UHI intensity based on temperature difference between the (a) PM IAG (suburban) and PM ITU (rural), (b) PM SFZ (urban) and PM ITU (rural), (c) PM IGEO (suburban) and INMET4 (rural), (d) INMET2 (urban) and INMET4 (rural), and (e) INMET3 (suburban) and INMET4 (rural). Thick red lines indicate the sunrise and sunset hours. Observation carried out from July 1, 2013 to December 1st, 2014.

January and August there is a secondary maximum during nighttime. The daytime maximum (~5.0°C) is largest in October (Figure 15a) when suburban site PM IAG is used as urban reference and the nighttime maximum (~6.0°C) in August (Figure 15b) when urban site PM SFZ is used as urban reference. This seasonal pattern differs from that found previously with only one maximum late in the afternoon[42,43]. The presence of secondary maximum during the night shows that UHI in

São Paulo may behave like in the cities located at higher latitudes. In this case the anthropogenic heat flux adopted here as valid for São Paulo by Ferreira et al.[40] is underestimated and needs to be reviewed.

In the MRRJ, the UHI intensity using PM IGEO and INMET2 as urban reference (Figure 1d) shows similar diurnal pattern with a daytime negative minimum and nighttime positive maximum. Using PM IGEO as urban reference the daytime minimum is ~ -1.0°C and

Original Research Article

the nighttime maximum ~ 2.5°C (Figure 15c). Using INMET2 as urban reference, a site closer to the ocean, a more intense daytime minimum (~ -5.0°C) and a nighttime maximum (~ 2.5°C) are observed, mainly during warmer months (Figure 15d). In the case of suburban reference INMET3, a site located 17 km far from the ocean, the minimum (~ -1.5°C) occurs at the dawn and the maximum (~ 1.5°C) at the evening and during the summer (Figure 15e).

In São Paulo the daytime minimum (~ 1.5°C using PM IAG as reference and ~ 0.5°C using PM SFZ as reference) is always positive. On the other hand, in Rio de Janeiro the daytime minimum is negative, reaching ~ -1.0°C using PM IGEO as urban reference and ~ -5.0°C using INMET2 as urban reference. When INMET3 (LCZ 6) is used as urban reference the daytime minimum is negative only during the winter months (Figure 15e).

These results indicate that in coastal cities that sea breeze cooling effect is as important as surface features in defining the pattern of urban anomalies in the temperature field so that the maximum positive UHI early in the morning becomes negative during the rest of the day[2]. In the case of São Paulo, 60 km far from the ocean, the sea breeze effect modulates daytime evolution of the UHI, but surface effects are predominant. Another factor that may systematically increase the UHI intensity is that the air temperatures used as a reference of rural areas were taken at the PM ITU, a site located in the southern edge of the Paulista Plateau (Figure 1c,e). The air temperature in the region of PM ITU is likely to be more affected by cold and moisture advections caused by sea-breeze circulation. In addition, the high frequency of fog in the PM ITU region may systematically reduce the solar heating early in the morning and late in the afternoon. All these preliminary results will have to be investigated further in order to clarify the mechanism that regulated the behavior of the UHI in these metropolitans' regions. For instance, the altitude correction performed in PM SFZ and PM IAG based on extrapolation of dry adiabatic lapse rate down to the surface will be investigated and presented in a future work by considering observations using a meteorological station set up at the surface in the site PM SFZ.

Urban boundary layer

Time evolution of the potential temperature, specific humidity, wind speed and direction profiles observed during daytime (06:00-18:00 LT) in the MRSP on February 20, 2013 (1st Campaign – summer) and August 8, 2013 (4th Campaign – winter), and in the MRRJ on July 12, 2013 (3rd Campaign – winter) are indicated in the Figure 16. They exemplify the daytime UBL evolution observed under undisturbed condition during summer and winter campaigns in the MRSP and MRRJ.

In the MRSP the UBL height, easily identified by visual inspection of potential temperature profiles as the top of the mixing layer, reached 2166 m at the end of the day on February 20 (Figure 16a). The top of the mixing layer can also be identified visually by the sharp drop in the vertical profile of the specific humidity (Figure 16b). On this day a Low-Level Jet (LLJ) blowing from NE was observed early in the morning (06:00 LT) at 357 m with intensity of 4.7 ms^{-1} (Figure 16c). The mixing effects due to daytime convective turbulence are noticeable in the wind speed and wind direction profiles (Figure 16c,d). During the winter campaign, the UBL height reached approximately 1436 m at 15:00 LT on August 8 (Figure 16i,j). An LLJ was also observed in the morning soundings (Figure 16g) with a maximum intensity of 12.8 m s^{-1} at 515 m and blowing from NE (Figure 16h). During winter in São Paulo turbulent mixing is strong enough to dilute the nocturnal LLJ that propagates upwards as the mixing layer increases (Figure 16k,l). In the MRRJ the UBL height reached approximately 488 m at 15:00 LT on July 12 (Figure 16e). The convective turbulent mixing does not seem to be strong enough to homogenize the mixing layer (Figure 16f). An LLJ was observed in the morning with intensity of 8.4 m s^{-1} (Figure 16g) at 917 m and blowing from N (Figure 16h).

The time evolution of the daytime UBL height and nighttime surface inversion layer thickness on February 20, 2013, July 12, 2013 and August 8, 2013 are indicated in Figure 17. The daytime UBL heights estimated from the air temperature gradient method are comparable with the ones obtained from the Lidar, located at approximately 1 km from the PM IAG, in the summer campaign (Figure 17a). Diurnal evolution of sensible heat flux observed during both experiments is indicated in Figure 17c,d. In both days the diurnal

Original Research Article

evolution of the sensible heat flux follows the diurnal evolution of the 10-days average values, indicating that they are representative of mean behavior of *H* during these three field campaigns.

There is an excellent agreement between UBL height and surface inversion layer estimates using the rawinsonde data (air temperature gradient method) and visual inspection during February 20 (Figure 17a) and August 8 (Figure 17e) in the MRSP. Similarly, a good agreement is observed in the MRRJ during July 12

(Figure 17b). The Lidar estimates of the UBL height agree very well with the rawinsonde estimates during the morning period and underestimate them during the afternoon on February 20 (Figure 17a). The agreement in the winter day in MRSP is much better than in the summer example. The vertical evolution of the UBL observed in the MRSP during these campaigns are consistent with the diurnal evolution of the sensible heat fluxes observed in the PM IAG with higher UBL in the summer campaign (Figure 17a,e) associated to higher
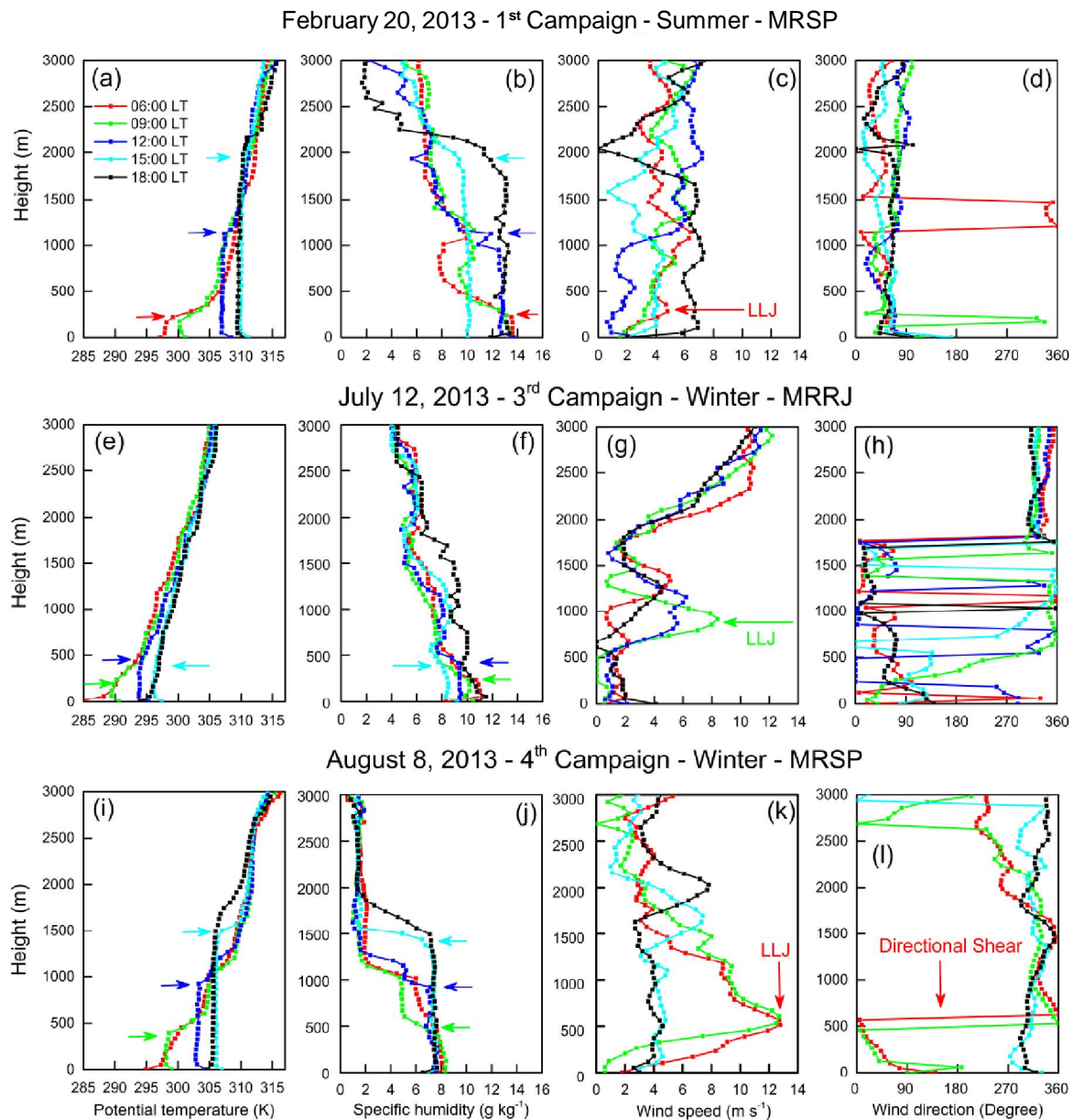

Figure 16 : Diurnal evolution of potential temperature, specific humidity, wind speed and wind direction based on rawinsonde carried out during daytime on (a)-(d) February 20, 2013 (1ˢᵗ Campaign), and (e)-(f) August 8, 2013 (4ᵗʰ Campaign), carried out at the *Campo de Marte* airport, located in the Metropolitan Region of São Paulo. The top of the UBL and LLJ are indicated by arrows.

Original Research Article

February 20, 2013 - 1st Campaign - Summer MRSP

July 12, 2013 - 3rd Campaign - Winter MRRJ

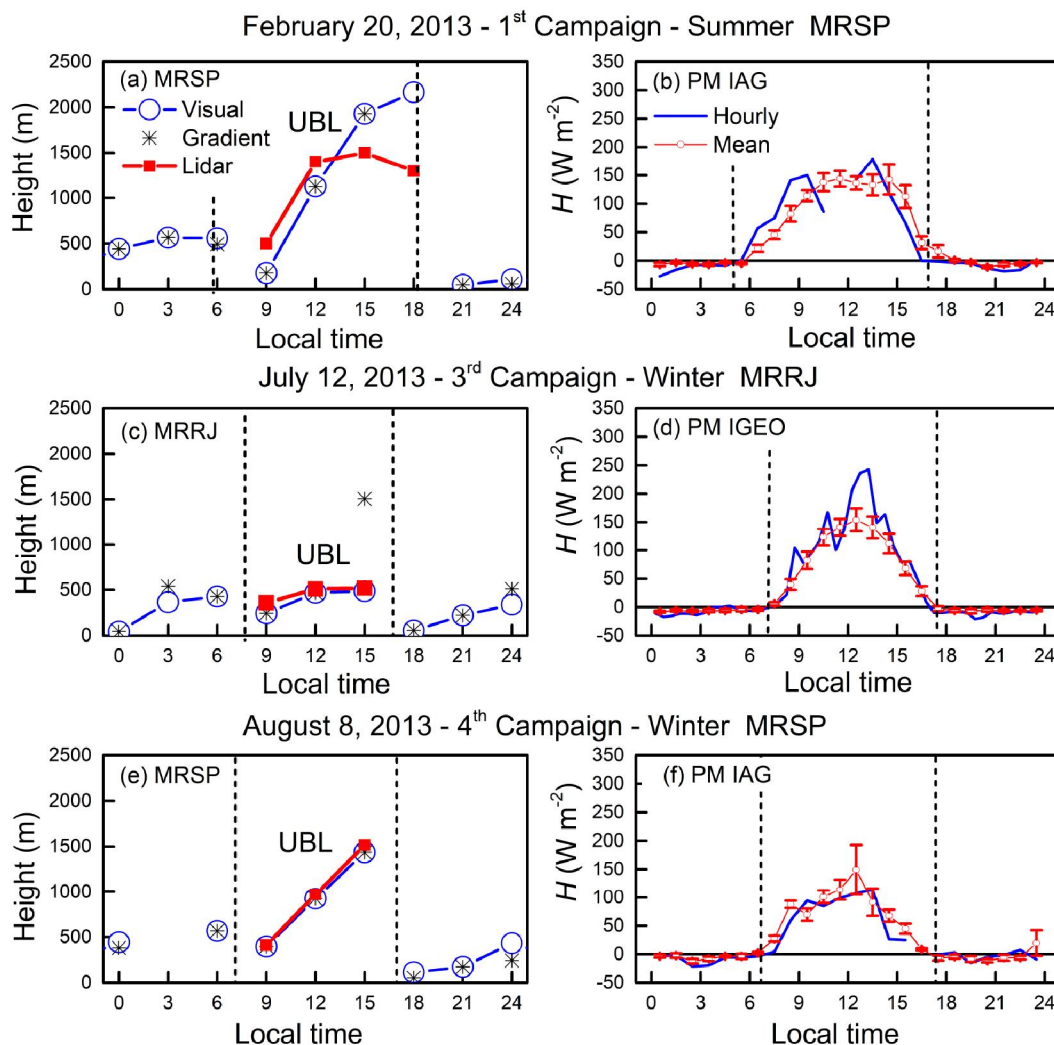## August 8, 2013 - 4th Campaign - Winter MRSP

Figure 17 : Diurnal evolution of UBL height, surface inversion layer top and sensible heat flux at the surface on: (a)- (b) February 20, 2013 -1st Campaign RMSP, (c)-(d) July 12, 2013 -3rd Campaign -RMRJ and (e)-(f) August 8, 2013 -4th Campaign -RMSP. Estimated from rawinsonde by temperature gradient (Gradient) method and Lidar. Visual estimates are also indicated (Visual). Sensible heat flux based from turbulence measurements carried in PM IAG and PM IGEO are indicated by blue solid circle line (hourly values) and red open circle line (mean hourly values during 10-days campaigns). Vertical bars indicate statistic error.

sensible heat flux magnitudes (Figure 17b,f). During the winter campaigns the UBL in the MRSP is higher than in the MRRJ (Figure 16c,d) although the magnitude of the sensible heat flux in the MRSP is smaller than in the MRRJ (Figure 17b,d). The behavior of the UBL in the MRRJ may be explained as sea breeze effect that transport shallower maritime PBL from relatively cold coastal oceanic waters during winter[35,103]. Sea-breeze circulation in this case is preventing the UBL to respond thermal convection caused by the solar heating of the surface where PM IGEO is located (Figure 6). During nighttime in both metropolitan regions a formation of shallow inversion layer during the early evening deepens

progressive to more than 500 m at dawn. Deep surface inversion layer in the MRSP associated to sea breeze effect is a common feature of the lower atmosphere during the end of daytime and early evening[104]. The observations analyzed here indicated that this effect remains during a longer period at nighttime in São Paulo.

These preliminary analyses of the urban effects on the climate in the MRSP and MRRJ indicate several features. Even though the agreement of the UBL height estimates displayed here is quite encouraging, these findings will have to be investigated in greater detail in a future work for both metropolitan regions by analyzing the entire set of data from all four field campaigns.

Original Research Article

SUMMARY AND CONCLUSIONS

The main goal of this work is to describe the implementation of the MCITY BRAZIL Project in the metropolitan regions of São Paulo and Rio de Janeiro. Observational studies about urban climate of Brazilian cities reviewed here indicated that most of the works available in the literature are limited to the analysis of conventional meteorological variables, mainly air and surface temperature, obtained by surface stations and satellite to monitor UHI intensity and its implications. They are concentrated in the southeast and south regions of Brazil, mainly São Paulo and Rio de Janeiro. Few works describe the vertical structure of the urban boundary layer, surface radiation and energy flux budgets, and none of them associates surface features with boundary layer properties and vice versa. The MCITY BRAZIL Project was designed to overcome the observational gap by assessing urban effects on the climate of the MRSP and MRRJ as a starting point and, systematizing this research so it can be extended to other urban areas in Brazil. In this work, it is presented a preliminary analysis for both metropolitan regions of: (a) Surface radiation balance; (b) Surface energy balance and turbulent fluxes; (c) Surface wind pattern; (d) Urban heat island; (f) Urban boundary layer. They were selected as key features in the identification of urban effects on the climate of cities in the context of the MCITY BRAZIL Project. This analysis is based on observations carried out from July 1st, 2013 to December 31st, 2014 in both metropolitan regions, including rawinsonde and Lidar measurements during field campaigns in 2013.

The analysis of the seasonal variation of SRB components, measured by the first time simultaneously in three sites in the MRSP and one site in the MRRJ, shows important differences. Considering as reference observations carried out in the suburban sites (PM IAG and PM IGEO) it is observed that the magnitude of SW_{DW} in the MRRJ is larger than in the MRSP. The magnitude of SW_{UP} follows the SW_{DW} because the albedo in the suburban areas of São Paulo and Rio de Janeiro are similar. These differences on SW components are linked to differences in the seasonal variation of cloud activity in these metropolitan regions, mainly in the summer. During winter higher pollution levels may contribute to increase the attenuation of SW_{DW} in São Paulo. The magnitudes of LW_{DW} and LW_{UP} in the MRRJ are systematically higher than in the MRSP. The behavior of both LW_{DW} and LW_{UP} are linked to differences in the surface temperature fields in these two metropolitan areas. As consequence of the differences in the SW and LW components, during daytime the magnitude of R_N in São Paulo is smaller (higher) than in Rio de Janeiro in the summer (winter). Within the MRSP all regional differences in the magnitude of SW and LW components are less significant, however the magnitudes of R_N are systematically higher (lower) during daytime (nighttime) in the rural area of the MRSP in both summer and winter.

The diurnal evolution of H and LE during the summer field campaigns in 2013 show a large magnitude in the MRSP. During the winter campaign the magnitude of H is larger in the MRSP however LE is larger in the MRRJ. Part of these differences is related to the presence of a large fraction of water in the case of Rio de Janeiro. The diurnal evolution of friction velocity in both metropolitan regions display daytime maximum and a nighttime minimum that is consistent with the diurnal evolution of the wind speed. The net daily CO_2 flux in the suburban area of the MRSP and MRRJ are larger during winter with values varying from 6.17 kg m^{-2} day^{-1} for São Paulo to 6.65 kg m^{-2} day^{-1} in Rio de Janeiro, indicating that despite the large fraction of vegetation other sources, mainly traffic of vehicle during rush hours in both regions and Guanabara bay in the case MRRJ, are contributing to CO_2 emission in this metropolitan regions. The SEB in the MRSP indicated that the residue, considered a surrogate for stored energy[43], is larger over urban and suburban areas.

The frequency distribution of wind intensity and direction at the surface in the MRSP is similar to the MRRJ, indicating that both regions are under the influence of similar large and mesoscale phenomena, modulated by local topography and land use. Sea breeze defines the diurnal evolution of wind speed and direction in both metropolitan regions. In the case of Rio de Janeiro, the complexity of coastline and the presence of Guanabara Bay make the sea breeze effects much more complex than in São Paulo. The diurnal evolution of the wind speed in both metropolitan regions displayed a daytime maximum and a nighttime minimum associated typical of flat regions.

Original Research Article

The seasonal evolution of the UHI intensity indicates a general pattern in both São Paulo and Rio de Janeiro with a daytime minimum and a nighttime maximum. In São Paulo, the daytime minimum is always positive, varies from 0.5 °C to 2.0 °C and occurs between 09:00 and 13:00 LT. A daytime local maximum varying from 3.5 °C and 5.0 °C and occurs in São Paulo between 14:00 and 17:00 LT. This daytime maximum extends throughout the night in January and August. In the Rio de Janeiro, the daytime minimum varies from -4.5 °C to 0.5 °C and occurs between 09:00 and 18:00 LT. The nighttime maximum varies from 1.5 °C to 2.5 °C and occurs between 18:00 and 09:00 LT. The UHI intensity decreases in São Paulo during daytime due to cooling effects caused by inland penetration of the sea breeze. In Rio de Janeiro, the maritime effect modulates the magnitude of the UHI so that during daytime areas far from coastline are warmer than closer areas, reducing or even changing the sign of the UHI intensity. During nighttime in both metropolitan regions the air temperature field responds predominantly to the urban heat exchange and UHI intensity remains positive most of the time.

The air temperature gradient and WTC methods used to estimate UBL height performed equally well for rawinsondes and Lidar monitoring in both metropolitan regions. The analysis of these estimates indicates that under undisturbed conditions, both UBL and surface inversion layer in São Paulo are deeper than in Rio de Janeiro. In São Paulo daytime UBL responds to the sensible heat flux at the surface. In Rio de Janeiro, UBL is smaller due to the internal maritime boundary layer effects. Despite the similar intensity and direction, the LLJ heights in São Paulo are shallower than in Rio de Janeiro.

It is important to emphasize that the results displayed here are preliminary and a more detailed investigation based on a more complete dataset (5 years) is being in progress. Besides, an important step towards the 5-year study in this paper such as land cover classification and EC post-processing tools were developed.

ACKNOWLEDGMENTS

REFERENCES

[1]   L.V.Abreu-Harbich, L.C.Labaki, A.Matzarakis; Theor.Appl.Climatol., **115**, 333-340 **(2014)**.

[2]   J.A.Acero, J.Arrizabalaga, S.Kupski, L.Katzschner; Theor.Appl.Climatol., **113**, 137-154 **(2013)**.

[3]   C.A.Alvares, J.L.Stape, P.C.Sentelhas, J.L.M.Gonçalves, G.Sparovek; Meteorol.Z., **22(6)**, 711-728 **(2014)**.

[4]   C.A.Alves, D.H.S.Duarte, F.L.T.Gonçalves; Energy Build., **114**, 62-71 **(2016)**.

[5]   M.F.Andrade, P.Kumar, E.D.Freitas, R.Y.Ynoue, J.Martins, L.D.Martins, T.Nogueira, P.Perez-Martinez, R.M.Miranda, T.Albuquerque, F.L.T.Gonçalves, B.Oyama, Y.Zhang; Atmos. Environ., **159**, 66-82 **(2017)**.

Original Research Article

[6] J.C.Antuña-Marrero, E.Landulfo, R.Estevan, B.Barja, A.Robock, E.Wolfram, P.Ristori, B.Clemesha, F.Zaratti, R.Forno, E.Armandillo, A.E.Bastidas, A.M.Frutos-Baraja, D.N.Whiteman, E.Quel, H.M.J.Barbosa, F.Lopes, E.Montilla-Rosero, J.L.Guerrero-Rascado; Bull.Am.Met. Soc., **98**, 1255-1275 **(2017)**.

[7] R.V.Araujo, M.R.Albertini, A.L.Costa-da-Silva, L.Suesdek, N.C.S.Franceschi, N.M.Bastos, G.Katz, V.A.Cardoso, B.C.Castro, M.L.Capurro, V.L.A.C.Allegro; Braz.J.Infect.Dis., **19(2)**, 146-155 **(2015)**.

[8] A.J.Arnfield; Int.J.Climatol., **23**, 1-26 **(2003)**.

[9] E.S.Assis, A.B.Frota; Atmos.Environ., **33**, 4135-4142 **(1999)**.

[10] M.Aubinet, T.Vesala, D.Papale; Eddy Covariance: A Practical Guide to Measurement and Data Analysis, Springer, Dordrecht, Netherlands, **(2012)**.

[11] H.Baars, A.Ansmann, R.Engelmann, D.Althausen; Atmos.Chem.Phys., **8**, 7281-7296 **(2008)**.

[12] D.H.Bando, C.T.Teng, F.M.Volpe, E.Mais, L.A.Pereira, A.L.Braga; Rev.Bras.Psiquiatr., **39**, 220-227 **(2017)**.

[13] E.W.Bárbaro, A.P.Oliveira, J.Soares, G.Codato, M.J.Ferreira, P.Mlakar, M.Z.Božnar, F.J.Escobedo; J.Appl.Meteor.Climatol., **49(12)**, 2574-2590 **(2010)**.

[14] E.C.Barboza, A.J.Machado; International Scholarly and Scientific Research & Innovation, **9(10)**, 1179-1182 **(2015)**.

[15] J.Barlow, M.Best, S.Bohnenstengel, P.Clark, C.S.B.Grimmond, H.Lean, A.Christen, S.Emeis, M.Haeffelin, I.Harman, A.Lemonsu, A.Martilli, E.Pardyjak, M.Rotach, S.Ballard, I.Boutle, A.Brown, X.Cai, M.Carpentieri, O.Coceal, B.Crawford, S.Di Sabatino, J.Dou, D.Drew, J.Edwards, J.Fallmann, K.Fortuniak, J.Gornall, T.Gronemeier, C.Halios, D.Hertwig, K.Hirano, A.Holtslag, Z.Luo, G.Mills, M.Nakayoshi, K.Pain, K.Schlünzen, S.Smith, L.Soulhac, G.Steeneveld, T.Sun, N.Theeuwes, D.Thomson, J.Voogt, H.Ward, Z.Xie, J.Zhong; Bull.Am.Met.Soc., OCTOBER 2017, Meeting Summaries, ES261-ES266 **(2017)**.

[16] J.F.Barlow; Urban.Climate, **10**, 216-240 **(2014)**.

[17] H.R.Barros, M.A.Lombardo; Heat island in the city of São Paulo - Thermal fields of Parks. LAP Lambert Academic Publishing, Saarbrücken, Germany, **(2016)**.

[18] B.Bechtel, C.Daneke; IEEE J.Sel.Top.Appl.

Earth Obs.Remote Sens., **5**, 1191-1202 **(2012)**.

[19] B.Bechtel, P.J.Alexander, J.Böhner, J.Ching, O.Conrad, J.Feddema, G.Mills, L.See, I.Stewart; ISPRS Int.J.Geoinf, **4**, 199-219 **(2015)**.

[20] A.K.Betts, J.J.H.Ball; Geophys.Res.Atmos., **102(D24)**, 28901-28909 **(1997)**.

[21] S.I.Bohnenstengel, I.Hamilton, M.Davies, S.E.Belcher; Q.J.R.Meteorol.Soc., **140**, 687-698 **(2014)**.

[22] V.Bourscheidt, O.Pinto Jr., K.P.Naccarato; J. Geophys.Res.Atmos., **121(9)**, 4429-4442 **(2016)**.

[23] Campbell; IRGASON Integrated CO2/H2O, Open-Path Gas Analyzer and 3D Sonic Anemometer, Revision 8/17. User Manual, Campbell Scientific Inc., **(2015)**.

[24] R.S.Cardoso, L.P.Dorigon, D.C.F.Teixeira, M.C.C.T.Amorim; Climate, **5**, 2-14 **(2017)**.

[25] J.Ching, G.Mills, B.Bechtel, L.See, J.Feddema, X.Wang, C.Ren, O.Brousse, A.Martilli, M.Neophytou, P.Mouzourides, I.Stewart, A.Hanna, E.Ng, M.Foley, P.Alexander, D.Aliaga, D.Niyogi, A.Shreevastava, S.Bhalachandram, V.Masson, J.Hidalgo, J.Fung, M.F.Andrade, A.Baklanov, D.D.Wei, G.Milcinski, M.Demuzere, N.Brunsell, M.Pesaresi, S.Miao, F.Chen; Bull. Amer.Meteor.Soc., **99**, 1907-1924 **(2017)**.

[26] G.Codato, A.P.Oliveira, J.Soares, J.F.Escobedo, E.M.Gomes, A.Dal Pai; Theor.Appl.Climatol., **93(1-2)**, 57-73 **(2008)**.

[27] L.C.Cotovicz Jr., B.A.Knoppers, N.Brandini, S.J.Costa Santos, G.Abril; Biogeosciences, **1(20)**, 6125-46 **(2015)**.

[28] B.Crawford, C.S.B.Grimmond, A.Christen; Atmos.Environ., **45**, 896-905 **(2011)**.

[29] A.D'Avignon, F.A.Carloni, E.L.La Rovere, C.B.S.Dubeux; Energy Policy, **38**, 4838-4847 **(2010)**.

[30] V.da Silva, P.V.de Azevedo, R.S.Brito, J.H.B.C.Campos; Environ.Monit.Assess., **161**, 45-59 **(2010)**.

[31] E.M.de Jesus, R.P.Rocha, M.S.Reboita, M.Llopart, L.M.M.A.Dutra, A.R.C.Remedio; Clim.Res., **68(2-3)**, 243-255 **(2016)**.

[32] H.A.R.De Bruin, A.Verhoef; Bound.-Layer Meteorol., **82**, 159-164 **(1997)**.

[33] M.A.F.S.Dias, J.Dias, L.M.V.Carvalho, E.D.Freitas; Clim.Change, **116**, 705-722 **(2013)**.

[34] D.Dodman; Environ.Urban., **21(1)**, 185-201 **(2009)**.

Original Research Article

[35] M.S.Dourado, A.P.Oliveira; Atmosfera, **21(1)**, 13-34 **(2008)**.

[36] D.H.S.Duarte, P.Shinzato, C.S.Gusson, C.A.Alves; Urban Clim., **14**, 224-239, **(2016)**.

[37] W.R.G.Farias, O.Pinto Jr., K.P.Naccarato, L.R.C.A.Pinto; Atmos.Res., **91**, 485-490 **(2009)**.

[38] W.R.G.Farias, O.Pinto Jr., I.R.C.A.Pinto, K.P.Naccarato; Atmos.Res., **135(136)**, 370-373 **(2014)**.

[39] N.F.Fernandes, R.F.Guimarães, R.A.T.Gomes, B.C.Vieira, D.R.Montgomery, H.Greenberg; Catena, **55**, 163-181 **(2004)**.

[40] D.G.Ferreira, C.M.O.Ferreira, E.S.Assis; Anais do XVI Congresso Brasileiro de Meteorologia, Belém, Pará, Brazil, September 13-17, 2010, 1, 1-5 **(2010)**.

[41] M.J.Ferreira, A.P.Oliveira, J.Soares; Theor.Appl. Climatol., **104**, 43-56 **(2011)**.

[42] M.J.Ferreira, A.P.Oliveira, J.Soares, G.Codato, E.W.Bárbaro, J.F.Escobedo; Theor.Appl. Climatol., **107(1)**, 229-246 **(2012)**.

[43] M.J.Ferreira, A.P.Oliveira, J.Soares; Urban Clim., **5**, 36-51 **(2013)**.

[44] J.J.Finnigan; Bound.-Layer Meteorol., **113(1)**, 1-41 **(2004)**.

[45] J.L.Flores Rojas, A.J.Pereira Filho, H.A.Karam, F.Vemado, V.Masson; Bound.-Layer Meteorol., **166**, 83-11 **(2018)**.

[46] J.L.Flores Rojas, A.J.Pereira Filho, H.A.Karam; Urban Clim., **17**, 32-66 **(2016)**.

[47] K.Fortuniak, W.Pawlak, M.Siedlecki; Bound.-Layer Meteorol., **146**, 257-276 **(2013)**.

[48] E.D.Freitas, M.R.Christopher, W.R.Cotton, P.L.S.Dias; Bound.-Layer Meteorol., **122(1)**, 43-65 **(2007)**.

[49] M.G.Giometto, A.Christen, C.Meneveau, J.Fang, M.Krafczyk, M.B.Parlange; Bound.-Layer Meteorol., **160(3)**, 425-452 **(2016)**.

[50] F.L.T.Gonçalves, P.L.S.Dias, G.P.Araújo; Int.J. Climatol., **22(12)**, 1511-1526 **(2002)**.

[51] M.J.Granados-Muñoz, F.Navas-Guzmán, J.A.Bravo-Aranda, J.L.Guerrero-Rascado, H.Lyamani, J.Fernández-Gálvez, L.Alados-Arboledas; J.Geophys.Res.Atmos., **117**, D18208 **(2012)**.

[52] C.S.B.Grimmond, T.S.King, M.Roth, T.R.Oke; Bound.-Layer Meteor., **89**, 1-24 **(1998)**.

[53] C.S.B.Grimmond, T.R.Oke; J.Appl.Meteorol., **38**, 922-940 **(1999)**.

[54] E.A.Haddad, E.Teixeira; Habitat Intern., **45(2)**, 106-113 **(2015)**.

[55] S.R.Hanna, J.C.Chang; Bound.-Layer Meteor., **58**, 229-259 **(1992)**.

[56] S.Q.S.Hirashima, E.S.Assis, M.Nikolopoulou; Build Environ., **107**, 245-253 **(2016)**.

[57] S.Q.S.Hirashima, A.Katzschner, D.G.Ferreira, E.S.Assis, L.Katzschner; Urban Clim., **23**, 219-230 **(2017)**.

[58] C.-I.Hsieh, G.Katul, T.-W.Chi; Adv.Water Resour., **23**, 765-772 **(2000)**.

[59] J.C.Hunt, Y.V.Timoshkina, S.I.Bohnenstengel, S.Belcher; Proc.Inst.Civ.Eng.Urban Des.Plan., **166(DP4)**, 241-254 **(2013)**.

[60] IBGE; Brazilian Institute of Statistics and Geography-Cities, https://cidades.ibge.gov.br/; Accessed 4 March 2020, **(2018)**.

[61] INMET; Brazilian Institute of Meteorology network. Technical information on the surface station network, http://www.inmet.gov.br/portal/ index.php?r=estacoes/estacoesAutomaticas; Accessed 4 March 2020, **(2019)**.

[62] M.Iqbal; An Introduction to Solar Radiation, Academic Press, Toronto, Canada, **(1983)**.

[63] S.Jochner, M.Alves-Eigenheer, A.Menzela, L.P.C.Morellato; Int.J.Climatol., **33**, 3141-3151 **(2013)**.

[64] M.Kanda; J.Meteor.Soc.Japan, **85B**, 363-383 **(2007)**.

[65] N.Kljun, P.Calanca, M.W.Rotach, H.P.Schmid; Geosci.Model.Dev., **8**, 3695-3713 **(2015)**.

[66] A.V.Kovalev, E.W.Eichinger; Elastic Lidar: Theory, Practice and Analysis Methods, Willey Interscience, New Jersey, USA, **(2004)**.

[67] E.Kruger; Landsc.Urban Plan., **134**, 147-156 **(2015)**.

[68] E.Kruger, C.Tamura; Energy and Emission Control Technologies, **2015(3)**, 55-66 **(2015)**.

[69] J.Kutzbach; MSc thesis, University of Wisconsin, Madison, USA, **(1961)**.

[70] E.Landulfo, C.A.Matos, A.S.Torres, P.Sawamura, S.T.Uehara; Atmos.Res., **85**, 98-111 **(2007)**.

[71] M.Y.Leclerc, T.Foken; Footprints in Micrometeorology and Ecology, Springer-Verlag, Heidelberg, Germany, **(2014)**.

[72] A.Lemonsu, V.Viguié, M.Daniel, V.Masson; Urban Clim., **14**, 586-605 **(2015)**.

[73] D.Li, E.Bou-Zeid, M.Oppenheimer; Environ.Res. Lett., **9(0555002)**, **(2014)**.

[74] G.N.Lima, V.O.M.Rueda; Weather.Clim.Extremes, **21**, 17-26 **(2018)**.

Original Research Article

[75] W.P.Lowry; J.Appl.Meteor., **16(2)**, 129-135 **(1977)**.

[76] A.J.Lucena, O.C.Rotunno Filho, J.R.França, L.F.Peres, L.N.R.Xavier; Theor.Appl.Climatol., **111**, 497-511 **(2013)**.

[77] R.W.Macdonald, R.F.Griffiths, D.J.Hall; Atmos. Environ., **32**, 1857-1864 **(1998)**.

[78] J.A.Marengo, S.C.Chou, R.R.Torres, A.Giarolla, L.M.Alves, A.Lyra; CCAFS Working Paper no. 73, CGIAR Research Program on Climate Change, Agriculture and Food Security (CCAFS). Copenhagen, Denmark, **(2014)**.

[79] G.L.Mariano, F.J.S.Lopes, M.P.P.M.Jorge; Atmos.Res., **98(2-4)**, 486-499 **(2010)**.

[80] E.P.Marques Filho, L.D.A.Sá, H.A.Karam, R.C.S.Alvalá, A.Souza, M.M.R.Pereira; Agric. For.Meteorol., **148**, 883-892 **(2008)**.

[81] E.P.Marques Filho, A.P.Oliveira, W.A.Vita, F.L.L.Mesquita, G.Codato, J.F.Escobedo, M.Cassol, J.R.A.França; Renew.Energ., **91**, 64-74 **(2016)**.

[82] V.Masson, C.Marchadier, L.Adolphe, R.Aguejdad, P.Avner, M.Bonhomme, G.Bretagne, X.Briottet, B.Bueno, C.de Munck, O.Doukari, S.Hallegatte, J.Hidalgo, T.Houet, J.Le Bras, A.Lemonsu, N.Long, M.-P.Moine, T.Morel, L.Nolorgues, G.Pigeon, J.-L.Salagnac, V.Viguié, K.Zibouche; Urban Clim., **10**, 407-429 **(2014)**.

[83] M.Mauder, T.Foken; Documentation and instruction manual of the eddy covariance software package TK3, University of Bayreuth, Bayreuth, Germany, **(2011)**.

[84] R.A.Menon, D.Y.C.Leung, L.Chunho; J.Environ. Sci., **20**, 121-138 **(2008)**.

[85] C.A.F.Monteiro; Urban Climatology and Its Applications with Special Regard to Tropical Areas, T.R.Oke, World Meteorological Organization, Geneva, Switzerland, **652**, 166-198 **(1986)**.

[86] O.L.L.Moraes; Bound.-Layer Meteorol., **96(3)**, 317-335 **(2000)**.

[87] K.N.Nair, E.D.Freitas, O.R.Sánchez-Ccoyllo, M.A.F.S.Dias, P.L.S.Dias, M.F.Andrade, O.Massambani; Meteorol.Atmos.Phys., **86(1-2)**, 87-98 **(2004)**.

[88] T.Nery, F.Pereira, R.Christensen; J.Climatol. Weather Forecasting, **3**, 134 **(2015)**.

[89] C.Nobre; Brazil and climate change: Vulnerability, impacts and adaptation, Center for Strategic Studies and Management (CGEE), Brasilia, Brazil, 11-18 **(2009)**.

[90] T.R.Oke; Boundary Layer Climates, Second Edition, Routledge, London, UK, **(1987)**.

[91] T.R.Oke; Initial guidance to obtain representative meteorological observations at urban sites. World Meteorological Organization Instruments and Observing Methods, 81 **(2006)**.

[92] A.P.Oliveira, J.Soares, T.Tirabassi, U.Rizza; Il Nuovo Cimento, **21C**, 631-647 **(1998)**.

[93] A.P.Oliveira, A.J.Machado, J.F.Escobedo, J.Soares; Theor.Appl.Climatol., **71(3-4)**, 231-249 **(2002)**.

[94] A.P.Oliveira, R.Bornstein, J.Soares; Water Air Soil Pollut., FOCUS 3, 3-15 **(2003)**.

[95] T.Oliveira, J.E.S.Sarkis, L.C.B.Menezes, J.C.Ulrich, P.M.G.Castro, A.J.Monteiro Jr, L.S.Maruyama, R.B.Yamaguishi; Proceedings of the International Nuclear Atlantic Conference - INAC 2013, Recife, PE, Brazil, November 24-29, 2013, **(2013)**.

[96] C.Park, G.W.Schade, N.D.Werner, D.J.Sailor; Atmos.Environ., **126**, 182-191 **(2016)**.

[97] E.Pereira, J.A.Baptista, B.J.Smith, J.J.McAllister; Annals of the Brazilian Academy of Sciences, **79(4)**, 739-750 **(2007)**.

[98] G.M.P.Peres, M.A.F.S.Dias; Int.J.Climatol., **37**, 1210-1220 **(2017)**.

[99] L.F.Peres, A.J.Lucena, O.C.Rotunno Filho, J.R.A.França; Int.J.Appl.Earth Obs.Geo-information, **64**, 104-116 **(2018)**.

[100] P.E.Phelan, K.Kaloush, M.Miner, J.Golden, B.Phelan, H.Silva, R.A.Taylor; Annu.Rev. Environ.Resour., **40**, 285-307 **(2015)**.

[101] O.Pinto Jr, I.R.C.A.Pinto; J.Geophys.Res., **113**, D20123 **(2008)**.

[102] M.R.Raupach, R.A.Antonia, S.Rajagopalan; Appl.Mec.Rev., **44**, 1-25 **(1991)**.

[103] F.N.D.Ribeiro, J.Soares, A.P.Oliveira; Bound.-Layer Meteorol., **158**, 139-150 **(2016)**.

[104] F.N.D.Ribeiro, A.P.Oliveira, J.Soares, R.M.Miranda, M.Barlage, F.Chen; Atmos.Res., **214**, 174-188 **(2018)**.

[105] M.C.Ribeiro, J.P.Metzger, A.C.Martensen, F.J.Ponzoni, M.M.Hirota; Biol.Cons., **142**, 1141-1153 **(2009)**.

[106] M.W.Rotach; Atmos.Environ., **33(24-25)**, 4001-4008 **(1999)**.

[107] M.W.Rotach, R.Vogt, C.Bernhofer, E.Batchvarova, A.Christen, A.Clappier, B.Feddersen, S.-E.Gryning, G.Martucci, H.Mayer, V.Mitev, T.R.Oke, E.Parlow, H.Richner, M.Roth, Y.-A.Roulet, D.Ruffieux, J.A.Salmond, M.Schatzmann, J.A.Voogt; Theor.Appl.Climatol., **81**, 231-261 **(2005)**.

Original Research Article

[108] M.Roth; Q.J.R.Meteorol.Soc., **126**, 941-990 (**2000**).

[109] M.Roth; Int.J.Climatol., **27**, 1859-1873 (**2007**).

[110] M.Roth, C.Jansson, E.Velasco; Int.J.Climatol., **37**, 2679-2698 (**2017**).

[111] M.P.Sánchez; MSc Thesis, University of São Paulo, São Paulo, Brazil, (**2017**).

[112] P.Seibert; Atmos.Environ., **34(7)**, 1001-27 (**2000**).

[113] N.Seino, T.Aoyagi, H.Tsuguti; Urban Clim., **23**, 8-35 (**2018**).

[114] F.B.Silva, K.M.Longo, F.M.Andrade; Environments, **4**, 27 (**2017**).

[115] J.M.Shepherd; Climate Vulnerability, Understanding and Addressing Threats to Essential Resources. R.A.Pielke, Elsevier Inc., USA, **5**, 109-125 (**2013**).

[116] H.R.Sobral; Crit.Public Health, **15(2)**, 147-156 (**2005**).

[117] C.Souch, C.S.B.Grimmond; Prog.Phys.Geogr., **30(2)**, 270-279 (**2006**).

[118] D.O.Souza, R.C.S.Alvalá; Meteorol.Appl., **21**, 186-193 (**2014**).

[119] I.D.Stewart, T.R.Oke; Bull.Am.Met.Soc., **93(12)**, 1879-1900 (**2012**).

[120] A.C.Targino, J.Soares; Atmos.Res., **63(1)**, 101-121 (**2002**).

[121] A.C.Targino, P.Krecl, G.C.Coraiola; Theor.Appl. Climatol., **117**, 73-87 (**2014**).

[122] C.F.B.Teixeira, L.C.Labaki; Intern.J.Renew. Sustain.Energy, **2(1)**, 12-17 (**2013**).

[123] UNESCO; United Nation Population Division, https://www.un.org/development/desa/publications/world-population-prospects-the-2017¬revision.html; Accessed 4 March 2020, (**2017**).

[124] E.Velasco, M.Roth; Geogr.Compass, **4(9)**, 1238-1259 (**2010**).

[125] F.Vemado, A.J.Pereira Filho; Adv.Meteorol., **2016**, 1-13 (**2016**).

[126] D.Vickers, L.Mahrt; J.Atmos.Oceanic Techno., **14(3)**, 512-526 (**1997**).

[127] J.M.Wilczak, S.P.Oncley, S.A.Stage; Bound.-Layer Meteorol., **99(1)**, 127-50 (**2001**).

[128] L.Yang, F.Qian, D.-X.Song, K.-J.Zheng; Procedia Eng., **169**, 11-18 (**2016**).

APPENDIX

Appendix A

TABLE A1 : Description of the sensors used in the MRSP and MRRJ between July 1st, 2013 and December 31st, 2014.

SRB components						
Sensor	**Platform**	**Operation period**	**Orientation**	**Height^a (m)**	**Height^{a1} (m agl)**	**location**
CNR4[#]	PM IAG	Dec 21, 2012 -Dec 31, 2014	Facing N	7.0	24.0	Tower$^\gamma$
	PM ITU	Apr 1, 2013 -Dec 31, 2014	Facing E	9.4	9.4	Tower$^{\gamma 1}$
	PM SFZ	July 1, 2013 -Dec 31, 2014	Facing SW	5.8	83.8	Tower$^{\gamma 2}$
	PM IGEO	Feb 4, 2013 -Dec 31, 2014	Facing NW	1.7	15.9	Pole$^{\gamma 3}$
H, LE, G, friction velocity and F$_{CO2}$						
Sensor	**Platform**	**Operation period**	**Orientation**	**Height (m)**	**Height (m agl)**	**position**
IRGASON[&]	PM IAG	Dec 21, 2012 -Dec 31, 2014	Facing S	8.4	25.4	Tower$^\gamma$
	PM ITU	Apr 1, 2013 -Dec 31, 2014	Facing W	9.6	9.6	Tower$^{\gamma 1}$
	PM SFZ	July 1, 2013 -Dec 31, 2014	Facing W	8.0	85.0	Tower$^{\gamma 2}$
	PM IGEO	Feb 4, 2013 -Aug 28, 2014	Facing N	8.5	22.7	Tower$^{\gamma 2}$
HFP01[*]	PM IAG	May 7, 2013 – Dec 31, 2014	-	-	-0.05	soil
	PM ITU	Apr 3, 2013 -Dec 31, 2014	-	-	-0.05	soil
Surface wind patterns						
Sensor	**Platform**	**Operation period**	**Orientation**	**Height (m)**	**Height (m agl)**	**Position**
034B[@]	PM IAG	Dec 21, 2012 -Dec 31, 2014	Facing SE	8.4	25.4	Tower$^\gamma$
	PM ITU	Apr 1, 2013 -Dec 31, 2014	Facing N	9.7	9.7	Tower$^{\gamma 1}$
	PM SFZ	July 1, 2013 -Dec 31, 2014	Facing NE	8.0	85.0	Tower$^{\gamma 2}$
	PM IGEO	Feb 4, 2013 -Aug 28, 2014	Facing N	6.0	20.2	Tower$^{\gamma 2}$

(TABLE A1 CONTINUE)

Original Research Article

			UHI			
Sensor	Platform	Operation period	Orientation	Height (m)	Height (m agl)	position
CS215[%]	PM IAG	Dec 21, 2012 - Dec 31, 2014	Facing S	1.7	18.7	Tower[γ]
	PM ITU	Apr 1, 2013 - Dec 31, 2014	Facing SE	1.6	1.6	Tower[γ1]
	PM SFZ	Jul 4, 2013 - Dec 31, 2014	Facing SE	1.6	78.6	Tower[γ2]
	PM IGEO	Feb 4, 2013 - Dec 31, 2014	Facing SE	3.0	17.2	Tower[γ2]
QMH102[$]	INMET2 INMET3 INMET4	May 20, 2011 - Dec 31, 2014	Not available	2.0	2.0	Pole[γ4]

[#] **Net radiometer, model CNR4, Kipp-Zonen Inc.** [&] **3D sonic anemometer, model IRGASON, Campbell Scientific Inc.** [*] **Soil Heat Fluxmeter, model HFP01, Campbell Scientific Inc.** [@] **3-cup anemometer and vane, model 034B MetOne Instruments Inc.** [%] **Temperature and relative humidity sensors, model CS215, CSI.** [$] **Temperature and relative humidity sensors, model QMH102, Vaisala. (TABLE 2).** [α] **Height above platform level.** [α1] **Height above ground level.** [γ] **10-m tower in the center of a concrete platform.** [γ1] **10-m tower at the surface.** [γ2] **10-m tower in the center of a metallic platform.** [γ3] **2-m pole located in the facade of the IGEO building.** [γ4] **4-m pole located at the surface**

TABLE A2 : Period of observations corresponding to the data used to characterize the climates of the MRSP and MRRJ.

Station	Temperature	Relative humidity	Wind speed	Precipitation
PEFI				
MIRANTE		1961 -1990		
INMET1				
PM IAG		Jul 1st, 2013-Dec 31st, 2014		
PM IGEO				

Appendix B

The local climate zones[119] was provided by the World Urban Database and Access Portal Tools (WUDAPT)[18,19]. Besides the LCZ, WUDAPT yields several geometric properties[25] with spatial resolution in the case of the MRSP and MRRJ of 300 m. TABLE B1 summarizes the geometric properties and LCZ classification for all sites. Corresponding landscape, land

TABLE B1 : Local climate zone (LCZ) for the MRSP and MRRJ.

	MRSP									
Site	Circular area (radius = 300 m)					Circular area (radius = 500 m)				
	Building height (m)				LCZ	Building height (m)				LCZ (Fraction %)
	Minimum	Maximum	Mean	Standard deviation		Minimum	Maximum	Mean	Standard deviation	
PM IAG	3.0	33.9	8.8	6.3	6	3.0	33.9	6.6	4.7	A(2.4), 6(97.6)
PM ITU	No buildings				A	No buildings				A
PM SFZ	2.9	108.7	15.9	16.9	1, 3, 8	2.9	108.7	16.4	16.3	1(33.2), 3(3.3), 8(63.4)
PEFI	2.7	21.7	4.9	3.2	A, 4	2.7	21.7	4.4	2.9	A(73.5), 4(22.8), 6(2.5), 9(1.1)
MIRANTE	2.8	50.9	6.5	5.4	3, 6	2.8	87.5	6.3	5.5	3(91.8), 6(6.6), 8(1.6)

	MRRJ									
Site	Circular area (radius = 300 m)					Circular area (radius = 500 m)				
	Building height (m)				LCZ	Building height (m)				LCZ (Fraction %)
	Minimum	Maximum	Mean	Standard deviation		Minimum	Maximum	Mean	Standard deviation	
PM IGEO	2.4	16.7	6.1	3.3	G, 3, 6, 8, 10	2.4	39.9	6.6	4.6	G(26.5), 3(4.3), 6(54.5), 8(10.5), 10(4,2)
INMET1	2.2	52.7	9.9	7.2	G, 3, 10	2.2	74.1	8.3	6.1	G(26.5), 1(1 3), 3(52.6), 10(19.7)
INMET2	2.3	75.6	21.0	16.1	G, 1	2.2	75.6	23.8	16.4	G(69.2), 1(30.8)
INMET3	2.8	6.1	3.8	0.9	3, 6	2.3	7.6	3.7	1.1	C(1.1), D(8.3), 3(32.2), 6(57.2), 10(1.2)
INMET4	No buildings				D, 6	No buildings				B(5.1), C(0.1), D(85.5), 6(9.3)

use and spatial distribution of LCZ classification for all surface weather stations are indicated in the Figure B1. The LCZ for each site is given by its predominance within 500-m radius circle area (Figures 3b, 6b and B1). For instance, LCZ 6 occurs in 97.6 % of this area around PM IAG, while LCZ A occurs in 73.5% of the area around PEFI (TABLE B1).

Appendix C

The land use classification, based on Ferreira et al.[43], indicates that the area within a circle of 1 km
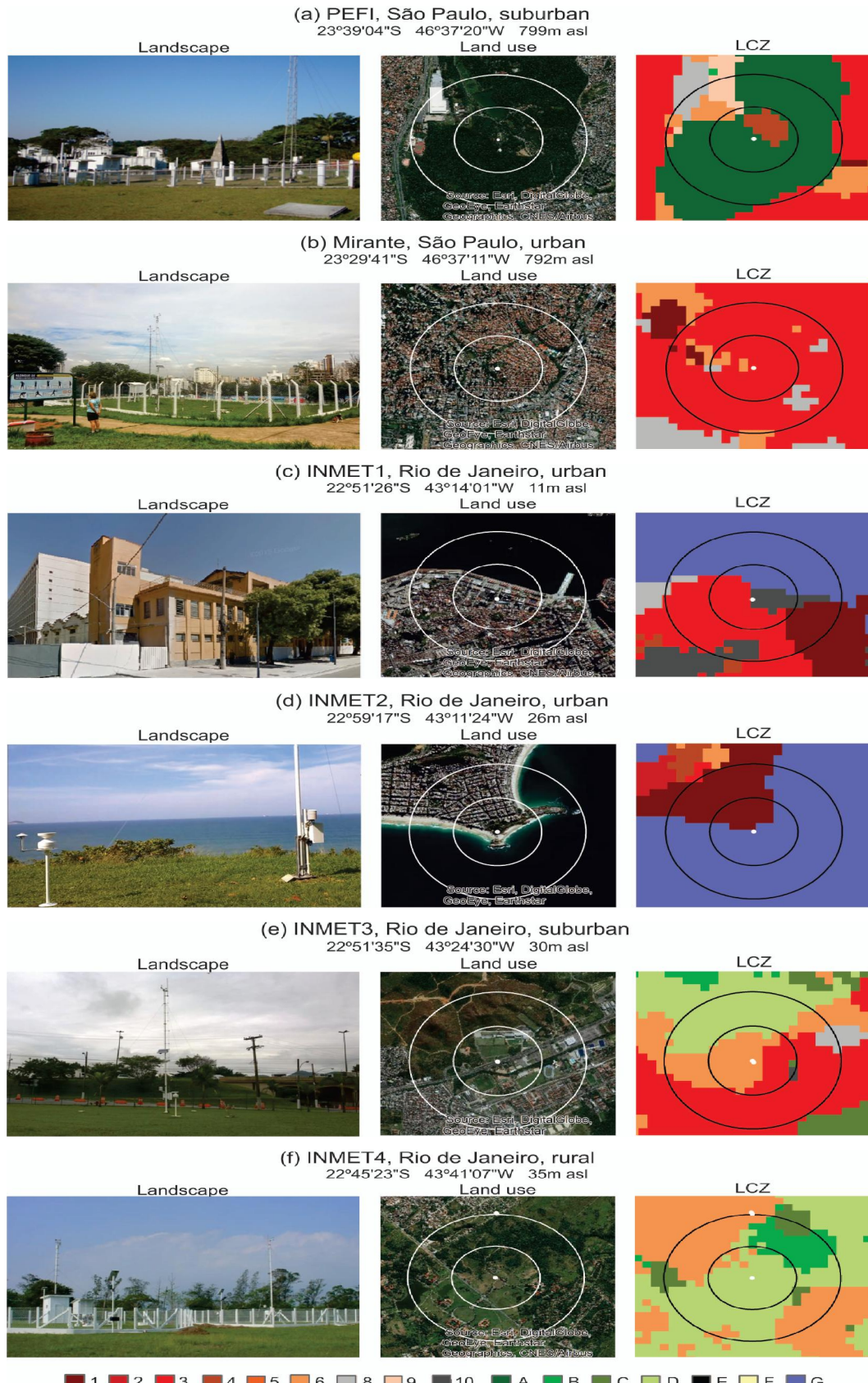
Original Research Article

Figure B1 : Landscape, land use and LCZ for surface weather stations located in the (a) MRSP and (b) MRRJ. White and black circles have a radius of 0.5 km and 1 km, respectively. (Google Earth June 1ˢᵗ, 2015).

Original Research Article

TABLE C1 : Land use characterization of the observational sites based on surface-type fractions (%) within 1-km and 3-km radius circles areas.

	Metropolitan Region of São Paulo									
	Site fraction (%) (Land use)									
	PM IAG (Suburban)		PM ITU (Rural)		PM SFZ (Urban)		PEFI (Suburban)		MIRANTE* (Urban)	
Surface type	23° 33' 34" S 46° 44' 01" W 744 m^A (17 m^B)		23° 49' 32" S 46° 30' 32'' W 760 m (0 m)		23 33' 01" S 46 37' 49" W 741 m (77 m)		23° 39' 04" S 46° 37' 20" W 799 m (0 m)		23° 29' 47"S 46° 37' 11" W 792 m (0 m)	
	1 km	3 km	1 km	3 km	1 km	3 km	1 km	3 km	1 km	3 km
Tree	25.4	5.5	87.6	69.9	5.6	2.8	83.5	28.4	5.7	7.0
Grass and herbaceous ground cover	6.6	2.0	2.0	1.2	3.6	0.6	2.0	1.0	0.0	0.0
Impervious building (roof)	15.1	78.0	0.4	0.5	45.2	87.5	7.2	52.8	87.4	86.2
Impervious road and street	49.0	11.1	1.6	2.4	43.4	8.6	0.4	14.2	6.8	6.7
Water	2.3	3.2	4.5	21.2	0.9	0.0	4.5	3.1	0.0	0.0
Soil and bare ground	0.9	0.1	1.0	0.0	1.3	0.2	0.0	0.0	0.0	0.0
Shrub and Scrub	0.7	0.1	2.9	4.8	0.0	0.3	2.4	0.5	0.1	0.1

	Metropolitan Region of Rio de Janeiro									
	Site fraction (%) (Land use)									
	PM IGEO (Suburban)		INMET1** (Urban)		INMET2& (Urban)		INMET3$ (Suburban)		INMET4# (Rural)	
Surface type	22° 51' 26" S 43° 14' 01" W 10 m (12.5 m)		22° 53' 43" S 43° 11' 11" W 11 m (0 m)		22° 59' 18" S 43° 11' 26" W 26 m (0 m)		22° 51' 41" S 43° 24' 41" W 30 m (0 m)		22° 45' 28" S 43° 41' 05" W 35 m (0 m)	
	1 km	3 km	1 km	3 km	1 km	3 km	1 km	3 km	1 km	3 km
Tree	14.9	7.5	2.1	3.4	2.1	4.5	21.4	34.9	19.4	13.9
Grass and herbaceous ground cover	10.3	2.7	0.4	1.2	0.2	0.4	15.6	9.1	56.3	55.0
Impervious building (roof)	29.6	33.3	31.4	20.2	25.0	13.5	34.8	40.6	18.1	24.9
Impervious road and street	17.4	17.8	23.3	21.3	8.2	5.9	7.6	6.9	2.4	3.5
Water	21.2	33.2	39.3	50.9	62.0	74.4	0.0	0.0	0.0	0.0
Soil and bare ground	6.5	5.4	3.5	3.0	2.5	1.3	12.3	7.1	2.1	0.3
Shrub and Scrub	0.1	0.1	0.0	0.0	0.0	0.0	8.3	1.4	1.7	2.4

(*) **MIRANTE** (*Mirante de Santana*); (**) **INMET1** (**Downtown**); (&) **INMET2** (*Copacabana*); ($) **INMET3** (*Deodoro*); (#) **INMET4** (*Seropédica Agrícola*). (A) **Above sea level (asl).** (B) **Above ground level (agl).**

(a) PM IAG

(b) PM ITU
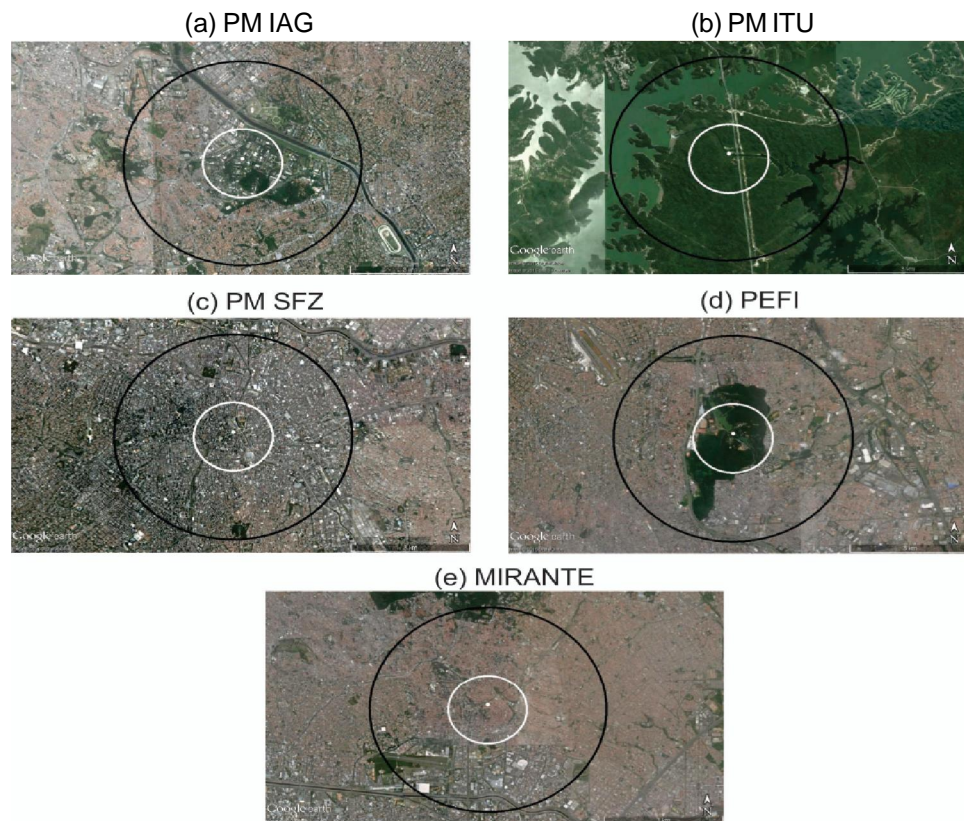
(c) PM SFZ

(d) PEFI

(e) MIRANTE

Figure C1 : Landscape and land use surface of the platforms (PM IAG, PM ITU, PM SFZ) and weather stations (PEFI, MIRANTE) located in the MRSP. White and black circles have a radius of 1 km and 3 km, respectively (Google Earth June 1st, 2015).
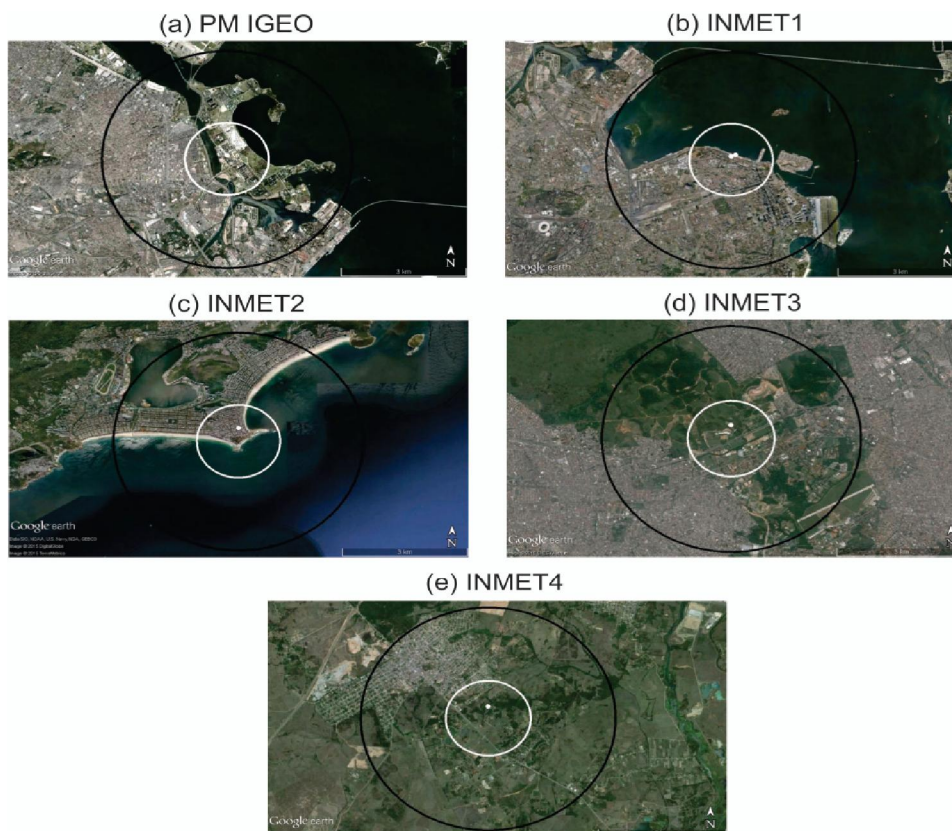
Original Research Article

Figure C2 : Landscape and land use surface of the PM IGEO and weather stations (INMET1-INMET4) located in the MRRJ. White and black circles have a radius of 1 km and 3 km, respectively (Google Earth June 1st, 2015).

around PM IAG (Figure C1a) has a suburban character (TABLE C1). The PM ITU (Figure C1b) is predominantly rural, while the PM SFZ is urban (Figure C1c). In the case of MRRJ, the classification indicates a suburban character for the PM IGEO (Figure C2a), despite the significant fraction (21.3%) of water. If the land use inventory area is increased to a circle with a 3-km radius (indicated by black circles in Figures 19-20), the land use of most sites changes considerably (TABLE C1). For example, the PM IAG becomes urban, since the area occupied by trees decreases from 25.4% to 5.5%. On the other hand, the PM ITU increases the fraction of surface occupied by water from 4.5% to 21.2% (TABLE C1). This land use classification is a valid alternative for urban areas where LCZ classification is not available.

Appendix D

To verify the performance of MBFlux, turbulent fluxes of sensible and latent heat, CO2 and friction velocity were estimated from turbulence observations carried out at the PM IAG on August 7, 2013 (year day 219) during the 4th Campaign in the MRSP. The performance of this algorithm was compared with the TK3 algorithm[83]. As can be seen in Figure D1, MBFlux performs well compared to TK3. The largest difference occurs during daytime for CO$_2$ flux.

To exemplify a typical outcome of the data quality control performed by the MBFlux, the fraction of the data problems is indicated in Figure D2 for turbulence observations carried out in the three platforms located in the MRSP during all field campaigns in 2013 and corresponding to four sets of 481 blocks of 30-minutes each. For the observations carried out at the PM IAG during the 1st and 4th campaigns, only 59.5% of the 962 blocks are considered valid (DATA-OK in Figure D2). During the 4th campaign, only 39% of the 481 blocks of data measured at the PM ITU are considered valid. The signal saturation caused by moisture deposition over the transducer and gas analyzer sensors (indicated by CAMPBELL in Figure D2) contributes the largest reduction in the dataset considered valid for the PM ITU. Observations gathered at the PM SFZ show the largest fraction of valid data (66.5%) for all the criteria used here.
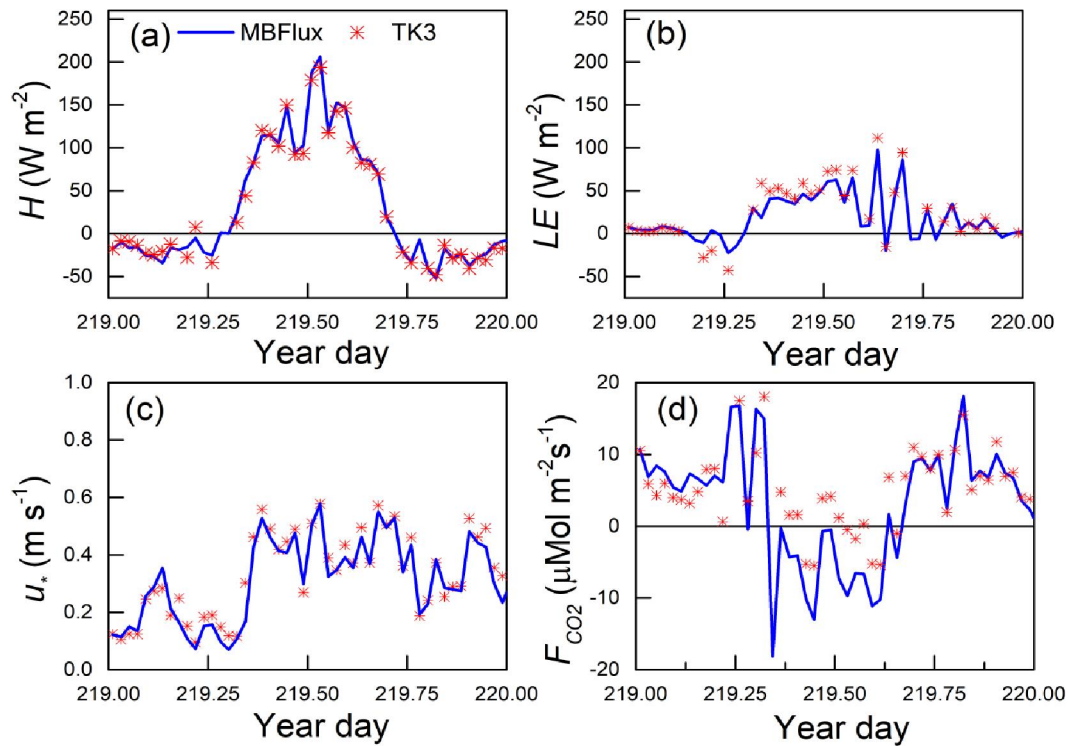
Original Research Article

Figure D1 : Time evolution of (a) sensible heat, (b) latent heat, (c) friction velocity and (d) vertical flux of CO_2 estimated by the MBFlux (blue line) and TK3 (red star). Observations carried out during August 7, 2013 (year day 219) in the 4th Campaign in MRSP at the PM IAG.
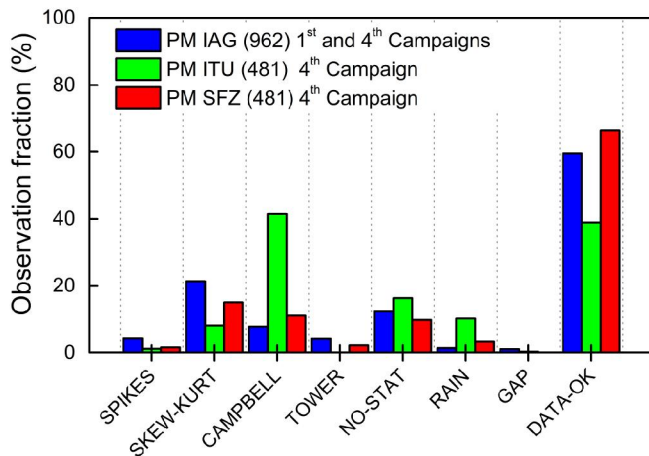

Figure D2 : Distribution of data removed by the data quality control procedure used in the MBFlux. SPIKES indicates data removed due to the presence of spikes, SKEW-KURT data outside of the skewness (-2, 2) and kurtosis (1, 8) thresholds intervals, TOWER is the data affected by the tower blocking effects; NO-STAT corresponds to the fraction of non-stationary blocks (Nonstationary Ratio >2) and RAIN is the fraction removed because it was affected by rain. GAP corresponds to the fraction of blocks removed because they have gaps larger than 15%. DATA-OK indicates the percentage of data accepted by all criteria.